LLNL-JRNL-843497

Observing the onset of the accretion wake in Vela X-1

C. M. Diez, V. Grinberg, F. Fuerst, I. El Mellah, M. Zhou, A. Santangelo, S. Martinez-Nunez, R. Amato, N. Hell, P. Kretschmar

December 24, 2022

Astronomy & Astrophysics

Disclaimer

Astronomy & Astrophysics manuscript no. output
June 30, 2023

Observing the onset of the accretion wake in Vela X-1

C. M. Diez[1], V. Grinberg[2], F. Fürst[3], I. El Mellah[4], M. Zhou[1], A. Santangelo[1], S. Martínez-Núñez[5], R. Amato[6], N. Hell[7], and P. Kretschmar[8]

[1] Institut für Astronomie und Astrophysik, Universität Tübingen, Sand 1, 72076 Tübingen, Germany
diez@astro.uni-tuebingen.de
[2] European Space Agency (ESA), European Space Research and Technology Centre (ESTEC), Keplerlaan 1, 2201 AZ Noordwijk, The Netherlands
[3] Quasar Science Resources S.L for European Space Agency (ESA), European Space Astronomy Centre (ESAC), Camino Bajo del Castillo s/n, 28692 Villanueva de la Cañada, Madrid, Spain
[4] Université Grenoble Alpes, CNRS, IPAG, Grenoble, France
[5] Instituto de Física de Cantabria (CSIC-Universidad de Cantabria), E-39005, Santander, Spain
[6] IRAP, CNRS, Université de Toulouse, CNES, 9 Avenue du Colonel Roche, 31028 Toulouse, France
[7] Lawrence Livermore National Laboratory, 7000 East Avenue, Livermore CA 94550, USA
[8] European Space Agency (ESA), European Space Astronomy Centre (ESAC), Camino Bajo del Castillo s/n, 28692 Villanueva de la Cañada, Madrid, Spain

Received 16 December 2022/ Accepted 16 March 2023

ABSTRACT

High-mass X-ray binaries (HMXBs) offer a unique opportunity to investigate accretion onto compact objects and the wind structure in massive stars. A key source for such studies is the bright neutron star HMXB Vela X-1 whose convenient physical and orbital parameters facilitate analyses and in particular enable studies of the wind structure in HMXBs. Here, we analyse simultaneous *XMM-Newton* and *NuSTAR* observations at $\phi_{\rm orb} \approx 0.36$–$0.52$ and perform time-resolved spectral analysis down to the pulse period of the neutron star based on our previous *NuSTAR*-only results. For the first time, we are able to trace the onset of the wakes in a broad 0.5–78 keV range with a high-time resolution of ∼283 s and compare our results with theoretical predictions. We observe a clear rise in the absorption column density of the stellar wind $N_{\rm H,1}$ starting at orbital phase ∼0.44, corresponding to the wake structure entering our line of sight towards the neutron star, together with local extrema throughout the observation, which are possibly associated with clumps or other structures in the wind. Periods of high absorption reveal the presence of multiple fluorescent emission lines of highly ionised species, mainly in the soft-X-ray band between 0.5 and 4 keV, indicating photoionisation of the wind.

Key words. X-rays: binaries, stars: neutron, stars: winds, outflows

1. Introduction

The prototypical eclipsing high-mass X-ray binary (HMXB) Vela X-1 is one of the brightest persistent point sources in the X-ray sky despite a moderate mean intrinsic luminosity of $5 \times 10^{36}\,\mathrm{erg\,s^{-1}}$ (Fürst et al. 2010). It lies at a relatively short distance of $1.99^{+0.13}_{-0.11}$ kpc; see the review by Kretschmar et al. (2021) and references therein for this and other system parameters quoted in Sect. 1. The system consists of a B0.5 Ib supergiant, HD 77581 (Hiltner et al. 1972), orbited by an accreting neutron star with an orbital period of ∼8.964 d (Kreykenbohm et al. 2008; Falanga et al. 2015). The mass and radius of HD 77581 have been estimated by different authors to be between ∼20 and ∼26 $M_\odot$ and between ∼27 and ∼32 $R_\odot$ (Table 4 in Kretschmar et al. 2021). A strong stellar wind with a mass-loss rate of $\sim 10^{-6} M_\odot\,\mathrm{yr^{-1}}$ (e.g. Watanabe et al. 2006; Falanga et al. 2015; Giménez-García et al. 2016) fuels the accretion of matter onto the neutron star and the pulsating X-ray emission with a fluctuating pulse period of ∼283 s. The mass of the neutron star is estimated to be ∼1.7–2.1 $M_\odot$, which is on the heavier side of the typical mass distribution; see Table 4 in Kretschmar et al. (2021), and especially the estimates by Rawls et al. (2011) and Falanga et al. (2015).

As the orbital separation of the two components is only $\sim 1.7\,R_\star$ (van Kerkwijk et al. 1995; Quaintrell et al. 2003), the neutron star is deeply embedded in the dense wind of the supergiant and significantly influences the wind flow. Due to the high inclination of the system of > 73° (Joss & Rappaport 1984; van Kerkwijk et al. 1995, and others), observations at different orbital phases can sample different structures in the stellar wind as modified by the interaction with the neutron star. One notable feature is the varying absorption as a function of orbital phase, which was detected by many authors (see the overview Fig. 5 of Kretschmar et al. 2021). They found a typical decrease in the absorption after eclipse up to an orbital phase of 0.2–0.3 (Martínez-Núñez et al. 2014; Lewis et al. 1992) followed by a sometimes steep increase in the phase range of 0.4–0.6 (Haberl & White 1990), with a varying location in phase in individual observations and with generally high absorption at later orbital phases (Sato et al. 1986; Haberl & White 1990).

In addition to the variations in observed flux due to X-ray absorption, wind-accreting X-ray pulsars also usually show significant variability of the intrinsic X-ray flux caused by a complex interplay of factors, such as variations in the density of the accreted material and possible inhibition of accretion by interactions at the magnetosphere. (Martínez-Núñez et al. 2017). For individual observations, especially at softer X-ray energies, it

is not always evident to distinguish absorption variations from those of the intrinsic emission. A study of variability in Vela X-1 by Fürst et al. (2010) based on *INTEGRAL* data in the hard X-ray band, which is only very slightly affected by absorption, found a log-normal distribution of the intrinsic flux values. On various occasions 'low states' or 'off-states' have been observed (see Table 1 in Kretschmar et al. 2021, with multiple references), but again not always with a clear distinction of intrinsic X-ray brightness versus high absorption.

Early on in the history of observations of this source, X-ray observations and optical-emission-line evidence suggested a wake structure trailing the X-ray source in the binary system (see references in Conti 1978). These structures can be caused by multiple processes. The neutron star moving highly supersonically through the dense stellar wind will lead to a bow shock with a trailing accretion wake. Photoionisation of the wind by the bright X-ray source can lead to the formation of a shock between the accelerating wind and the stalling photoionised plasma (Fransson & Fabian 1980), which can then lead to a trailing spiral structure, the photoionisation wake. X-ray heating and radiative cooling of the wind (Kallman & McCray 1982; Blondin et al. 1990) can create additional instabilities and filamentary structures, leading to stronger short-term variations. Tidal deformation of the mass donor can lead to enhanced wind flux in the direction of the neutron star, even if it does not fill its Roche Lobe. For close systems, this can develop into a dense 'tidal stream' (Blondin et al. 1991), which when deflected by coriolis force tends to pass behind the compact object, which explains the high absorption at later orbital phases. The density enhancement from such a tidal stream would be expected to be quite stable in orbital phase, while variations caused by an accretion wake would vary from orbit to orbit. According to Blondin (1994), in a specific system, there would be either a tidal stream between the star and the neutron star, or a photoionisation wake trailing the neutron star.

Vela X-1 has also been studied via X-ray line spectroscopy. Early studies (e.g. Becker et al. 1978; Ohashi et al. 1984) mainly focused on the pronounced iron-line complex visible also very clearly in eclipse. A broad FeKα emission line was also found by Sato et al. (1986), but these authors suspected further contributions to the overall line intensity from FeKβ as well as from fluorescent Kα lines of Si, S, Ar, Ca, and Ni. Further elements have been reported from spectra taken during or close to eclipse (Nagase et al. 1994; Sako et al. 1999; Schulz et al. 2002), including recombination lines and radiative recombination continua (RRC), as well as fluorescence lines. The variety of observed ionisation states is a strong indication of the presence of an inhomogeneous wind with optically thick, less ionised matter coexisting with warm photoionised plasma. *Chandra*/HETGS spectra from three orbital phases (0, 0.25 and 0.5) were analysed by Goldstein et al. (2004) and Watanabe et al. (2006), who found an eclipse-like spectrum around orbital phase 0.5, while the spectrum was dominated by the continuum around phase 0.25. Grinberg et al. (2017) revisited the observation at phase 0.25, analysing time intervals of low and high spectral hardness (i.e. different levels of absorption) separately and detected line features from high- and low-ionisation species of Si, Mg, and Ne, as well as strongly variable absorption. This again implied the presence of both cool and hot gas phases, possibly from the combination of an intrinsically clumpy stellar wind and a highly structured accretion flow close to the compact object. Analysing the grating spectrometer data of a long *XMM-Newton* observation at early orbital phases, Lomaeva et al. (2020) found emission lines corresponding to highly ionised O, Ne, Mg, and Si as well as RRC of O. In addition, these authors found potential absorption lines of Mg at a lower ionisation stage and features identified as iron L lines.

In our targeted observing programme with *XMM-Newton* and *NuSTAR*, we aimed to cover an interesting binary phase range in which we expect strong changes in absorption while the accretion and ionisation wakes are crossing the line of sight of the observer (Grinberg et al. 2017). In our previous work with *NuSTAR* (Diez et al. 2022), we observed strong absorption variability along the orbital phase. However, an in-depth study of the varying absorption cannot be explored with *NuSTAR* alone as we need coverage at lower energies, which is possible with *XMM-Newton*. On the other hand, *XMM-Newton* alone is not sufficient and we need *NuSTAR* to constrain the continuum, hence the necessity for simultaneous observation.

We introduce the datasets and their reduction in Sect. 2 followed by a presentation of the light curves extracted in different relevant energy bands in Sect. 3. Using the results, we proceed to the time-resolved spectral analysis in Sect. 4 and finally discuss our results in Sect. 5, focusing on the absorption variability. A summary is given in Sect. 6 and in Appendix A we describe the calibration issues we faced during this work between *NuSTAR* and *XMM-Newton* in detail.

2. Observation and data reduction

Vela X-1 was observed on 3–5 May 2019 as the science target of a simultaneous campaign with *XMM-Newton* and *NuSTAR*. We used the European Photon Imaging Camera pn-CCDs (EPIC-pn; Strüder et al. 2001), the EPIC Metal Oxide Semiconductor (EPIC-MOS; Turner et al. 2001), and the Reflection Grating Spectrometers (RGS; den Herder et al. 2001) on board *XMM-Newton* (Jansen et al. 2001) under Obs ID 0841890201. The *NuSTAR* data under Obs ID 30501003002 were analysed in Diez et al. (2022). In the present paper, we focus on the simultaneous analysis of the new EPIC-pn data with our previous *NuSTAR* work (updated with the current calibration files and software) in order to obtain a broadband mapping of the stellar wind along the orbital phase of the neutron star around the companion star. The simultaneous RGS data will be explored in a later work. Details about the observation are given in Table 1 and a sketch of the system during this observation is shown in Fig. 1. We note the much larger net *XMM-Newton* EPIC-pn exposure due to the low Earth orbit (LEO) of *NuSTAR*.

The orbital phases $\phi_{\rm orb}$ are obtained with the ephemeris in Table 2 from Diez et al. (2022), which is derived from Kreykenbohm et al. (2008) and Bildsten et al. (1997) and where $\phi_{\rm orb} = 0$ is defined as T_{90}. The time of phase zero is usually defined using T_{90} (the time when the mean longitude l is equal to 90°) or by $T_{\rm ecl}$ (the mid-eclipse time). Explanations on how to convert T_{90} to $T_{\rm ecl}$ can be found in Kreykenbohm et al. (2008). Table 1 also provides orbital phases with $T_{\rm ecl}$. In this work, we exclusively use T_{90} and all the mentioned times are corrected for the binary orbit.

We use HEASOFTv6.30.1, and to analyse the data, we use the Interactive Spectral Interpretation System (ISIS) v1.6.2-51 (Houck & Denicola 2000). ISIS provides access to XSPEC (Arnaud 1996) models that are referenced later in the text.

2.1. NuSTAR

We used the NuSTARDAS pipeline (`nupipeline`) v2.1.2 with the calibration database (CALDB) v20220608 applied with the

Table 1. Observations log.

Instrument	Obs ID	Time Start MJD (day) binarycor[(a)]	Time Stop MJD (day) binarycor[(a)]	Exposure (ks)	Orbital phase (with T_{90})	Orbital phase (with T_{ecl})
NuSTAR	30501003002	58606.8688	58608.2465	40.562	0.36–0.52	0.34–0.49
XMM-Newton	0841890201	58606.9283	58608.2146	109.311	0.37–0.51	0.34–0.48

[(a)] Stands for 'binary-corrected' times. The `BinaryCor` tool in ISIS removes the influence of the double-star motion for circular or elliptical orbits. The Git repository of the `isisscripts` where the `BinaryCor` function is described at https://www.sternwarte.uni-erlangen.de/gitlab/remeis/isisscripts/-/blame/6216a4ab8307f5825e17109db3cfb5c317a7ab08/share/isisscripts.sl. The start and stop times are given as modified Julian dates (MJD).

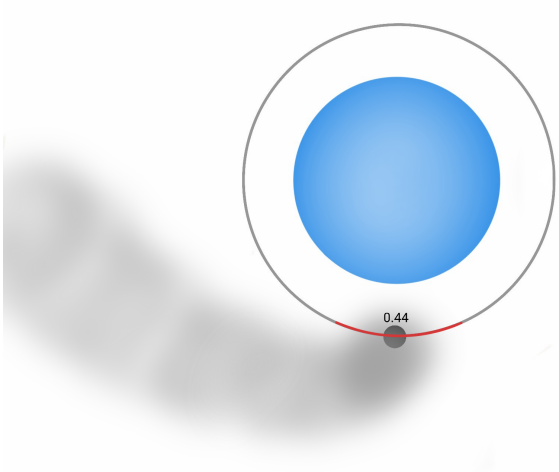

Fig. 1. Sketch of Vela X-1 showing the orbital phases covered during this *XMM-Newton* EPIC-pn observation. In this image, the observer is located facing the system at the bottom of the picture.

clock correction. We proceeded to the extraction of the products as in Diez et al. (2022), using the updated pipeline and calibration files mentioned above. Briefly, we extracted a spectrum for every orbit of *NuSTAR* around the Earth and for every rotation of the neutron star with the previously derived pulse period of ~283 s. For the extraction of the source region, we used a smaller radius of ~60 arcsec to minimise the impact of the background. The uncertainties are given at 90% confidence and the events were barycentred using the `barycorr` tool from the NUSTARDAS pipeline. The spectra were rebinned within ISIS to a minimal signal-to-noise ratio (S/N) of 5, adding at least 2, 3, 5, 8, 16, 18, 48, 72, and 48 channels for energies in the ranges 3.0–10, 10–15, 15–20, 20–35, 35–45, 45–55, 55–65, 65–76, and 76–79 keV, respectively, as in our previous work.

2.2. XMM-Newton

The observation was setup in pn-timing mode with a thin filter. For the generation of the event lists file, we used the Science Analysis System (SAS) software v20.0 with the Current Calibration Files (CCF) as of April 2022 starting from Observation Data Files (ODFs) level running `epproc`[1].

The default calibration uses `withrdpha='Y'` and `runepfast='N'` as of SASv14.0[2]. However, this default timing mode calibration led us to an offset of the instrumental and physical lines of the source towards higher energies of ~+140 eV (see Appendix A.1). Therefore, after consulting with the *XMM-Newton* calibration team (S. Migliari, priv. comm.), we decided to instead turn off the Rate-Dependent PHA (RDPHA) correction (`withrdpha='N'`) and apply the Rate-Dependent CTI (RDCTI) correction using `epfast` (`runepfast='Y'`), resulting in satisfactory spectra.

No filtering for flaring particle background was necessary. Because the source was so bright that it illuminated the whole CCD detector, no background was extracted. The event times were barycentred using the `barycen` tool from the SAS pipeline and were deleted if found to be on bad pixels with the `#XMMEA_EP` argument in the `evselect` step.

As *XMM-Newton* EPIC-pn and *NuSTAR* observations were simultaneous, we were able to reuse the pulse period previously derived on the FPMA light curve, $P = 283.4447 \pm 0.0004$ s (Diez et al. 2022), to extract the *XMM-Newton* light curves in order to avoid intrinsic pulse variability. For a sanity check, we still performed epoch folding on the *XMM-Newton* light curve with 1 sec binning and indeed derived the exact same pulse period as in our previous work.

We selected single and double pixel events (`PATTERN<=4` in the `evselect` step) in the source region from `RAWX=32` to `RAWX=44`. We removed the outermost parts of the point spread function (PSF) wings to reduce the influence of background noise or possible dust scattering effects. The count rate of the overall observation on different energy bands was sufficiently high to select a region of only 13 pixels centred around the maximum of the PSF. We applied the task `epiclccorr` to perform absolute and relative corrections.

2.3. Spectrum extraction and pile-up

For the extraction of the spectra, we performed the same selection of events as above, but we also deleted events close to CCDs gaps or bad pixels (`FLAG==0` in the `evselect` step). An update to the EPIC effective area was made available in April 2022 to improve the cross-calibration between *XMM-Newton* and *NuSTAR* as of April 5, 2022[3]. As we want to compare our *XMM-Newton* results to our previous *NuSTAR* ones, we activated this correction using the `applyabsfluxcorr=yes` argument in the `arfgen` step. All spectra were rebinned using the optimal rebinning approach of Kaastra & Bleeker (2016).

Because of the high count rate (see Sect. 3), the data were strongly affected by pile-up (Jethwa et al. 2015), in particular

[1] https://xmm-tools.cosmos.esa.int/external/sas/current/doc/epproc/node8.html

[2] see the *XMM-Newton* CCF Release Note 0369 (Migliari S., Smith M., 2019, XMM-CAL-SRN-0369) https://xmmweb.esac.esa.int/docs/documents/CAL-SRN-0369-0-0.pdf

[3] see the *XMM-Newton* Science Operations Team Calibration Technical Note 0230 (Fürst F., 2022, XMM-SOC-CAL-TN-0230) https://xmmweb.esac.esa.int/docs/documents/CAL-TN-0230-1-3.pdf

at the centre of the PSF. To test and evaluate for pile-up in our observation, we used the `epatplot` task to read the pattern information statistics of the input EPIC-pn set as a function of PI channel. As an additional sanity check, we performed an energy test on the iron line region (for more details, see Appendix A.2). According to the results of these tests, we decided to exclude the three centremost columns of the PSF (`RAWX 37-38-39`). Moreover, we excluded spectral channels below 0.5 keV and above 10 keV from the analysis where the S/N was very low.

We use this work to also report some cross-calibration issues between *NuSTAR* and *XMM-Newton* EPIC-pn. Cross-calibration issues between *XMM-Newton* EPIC-pn and *NuSTAR* are a known phenomenon when combining datasets from both observatories[3] (see e.g. Gokus 2017) and the *XMM-Newton* Science Operations Centre is working on this issue with an upcoming update of the SAS software (S. Migliari, private conversation). At the time of writing, no release is available, and so we describe the cross-instrumental issues in Appendix A.3 and how we coped with them for our analysis in Sect. 4.2.

3. Light curves and timing

3.1. Pulse period and average light curves

Strong flux variability was detected in Vela X-1 during this observation with timescales ranging from several kiloseconds down to the pulse period of the neutron star. To study the overall system behaviour, we present the 0.5–10 keV *XMM-Newton* EPIC-pn light curve in Fig. 2 together with the *NuSTAR* FPMA and FPMB 3 –78 keV light curves.

The ratio of the *XMM-Newton* EPIC-pn count rate by the *NuSTAR* FPMA-FPMB count rate is not constant. During the first half of the observation (until $T_{\rm obs} \approx 58607.60$ MJD), the average *XMM-Newton* EPIC-pn count rate is ∼30% higher than the *NuSTAR* one. Their ratio stabilises around 1 during the second half of the observation when the wakes are coming through our line of sight (see Fig. 1) and therefore when the absorption from the stellar wind is more prominent. As *XMM-Newton* EPIC-pn covers lower energies than *NuSTAR*, we expect it to be more affected by the absorption due to the stellar wind, explaining this behaviour.

All the major flares detected are indicated by arrows in Fig.2. We can observe three flares happening simultaneously with both *NuSTAR* and *XMM-Newton* EPIC-pn at $T_{\rm obs} \approx 58606.95$ MJD, $T_{\rm obs} \approx 58607.04$ MJD, and $T_{\rm obs} \approx 58607.42$ MJD, and a fourth flare visible at $T_{\rm obs} \approx 58608.23$ MJD covered by *NuSTAR* only, as expected in Diez et al. (2022). With the new addition of EPIC-pn data, we can retrieve the data between $T_{\rm obs} \approx 58607.57$ MJD and $T_{\rm obs} \approx 58607.76$ MJD, which were lost during the *NuSTAR* campaign, and also retrieve data during the eclipses of the *NuSTAR* instrument. Therefore, we can observe three new flares at $T_{\rm obs} \approx 58607.72$ MJD, $T_{\rm obs} \approx 58607.80$ MJD, and $T_{\rm obs} \approx 58607.93$ MJD, together with the flare at $T_{\rm obs} \approx 58607.42$ MJD, which is longer than what was seen with *NuSTAR*. This flare lasts ∼8 ks and reaches ∼300 counts s^{-1} which is almost as long as but brighter than the flaring period in Martínez-Núñez et al. (2014). The timescales of the flares appear to be from less than a *NuSTAR* eclipse (∼2.5 ks) up to ∼8 ks. The brightest observed flare at $T_{\rm obs} \approx 58607.04$ MJD reaches ∼465 counts s^{-1} with EPIC-pn.

3.2. Energy-resolved light curves

To estimate the influence of the stellar-wind absorption on the observed count-rate variations, we extract the light curves in the relevant energy bands. In Diez et al. (2022), we saw a change in the hardness ratio between the 3.0–5.0 keV and 20.0–30.0 keV energy bands, roughly separating the observation into three noticeable phases: stable hardness ratio from the beginning of the observation to $T_{\rm obs} \approx 58607.57$ MJD, followed by the loss of the *NuSTAR* data until $T_{\rm obs} \approx 58607.76$ MJD, and finally the rise of the hardness ratio until the end. Fig. 3 shows three different *XMM-Newton* EPIC-pn spectra taken during the above-mentioned phases of the observation. We can observe low-energy variability towards the end of the observation (last panel of the figure). As expected from the geometry of the system (see Fig. 1), when the wakes occupy most of the line of sight of the observer, the absorption from the wind is so strong that the emission lines of the material become visible (see e.g. Watanabe et al. 2006). From the last spectrum, we can even highlight four energy bands of interest. The first one, from 0.5 keV to 3.0 keV, covers all the low-energy emission lines. We choose the second energy band from 3.0 keV to 6.0 keV to account for the low-energy part of the continuum before the iron-line region from 6.0 keV to 8.0 keV. The last energy band covers the high-energy part of the continuum from 8.0 keV to 10.0 keV. This will help us to compare the photon count rate in different energy bands relative to the continuum to check for variability. We present a more detailed spectral analysis in Sect. 4.

We present the *XMM-Newton* EPIC-pn light curves in the above-mentioned energy bands in Fig. 4. All light curves show the same features and variability in all energy bands, but the flares and low states are more prominent at low energies, particularly in the 0.5–3.0 keV energy band where the brightest flare is approximately five times higher than the average count rate in that band (∼24 counts s^{-1}). We notice a corresponding trend for the low state at $T_{\rm obs} \approx 58607.24$ MJD, which is roughly five times smaller than the average count rate in the 0.5–3.0 keV band. The long and broad flare is visible in all energy bands but, again, is much more prominent in the 0.5–3.0 keV energy band and shows a rather stable plateau at ∼40 counts s^{-1}. In the two highest energy bands, the overall count rate stays relatively stable around the mean value of each individual light curve. This phenomenon was observed in a similar energy band, 1.0–3.0 keV, in Martínez-Núñez et al. (2014) and was associated with a stable spectral shape from the unabsorbed source.

3.3. Hardness ratios

For a more quantitative study of the source variability and in particular in an attempt to determine the origin of the variability shown in Vela X-1, we present the *XMM-Newton* EPIC-pn hardness ratios in Fig. 5. In the second panel, we observe a mirrored version of the light curve for the hardness ratio between the S = 0.5–3.0 keV and H = 8.0–10.0 keV bands. The minima of the hardness ratio correspond to the maxima of the light curve and vice versa. This shows that the observed flares of the light curve happen during the softening of the spectral shape, suggesting a contribution mainly from low-energy photons, as seen in Fig. 4. On the contrary, low states correspond to a hardening of the spectral shape, suggesting the major contribution is from high-energy photons. In the third panel, the hardness ratio between the S = 3.0–6.0 keV and H = 8.0–10.0 keV bands remains relatively constant until $T_{\rm obs} \approx 58607.60$ MJD ($\phi_{\rm orb} \approx 0.44$), with a local maximum at $T_{\rm obs} \approx 58607.24$ MJD ($\phi_{\rm orb} \approx 0.40$). The over-

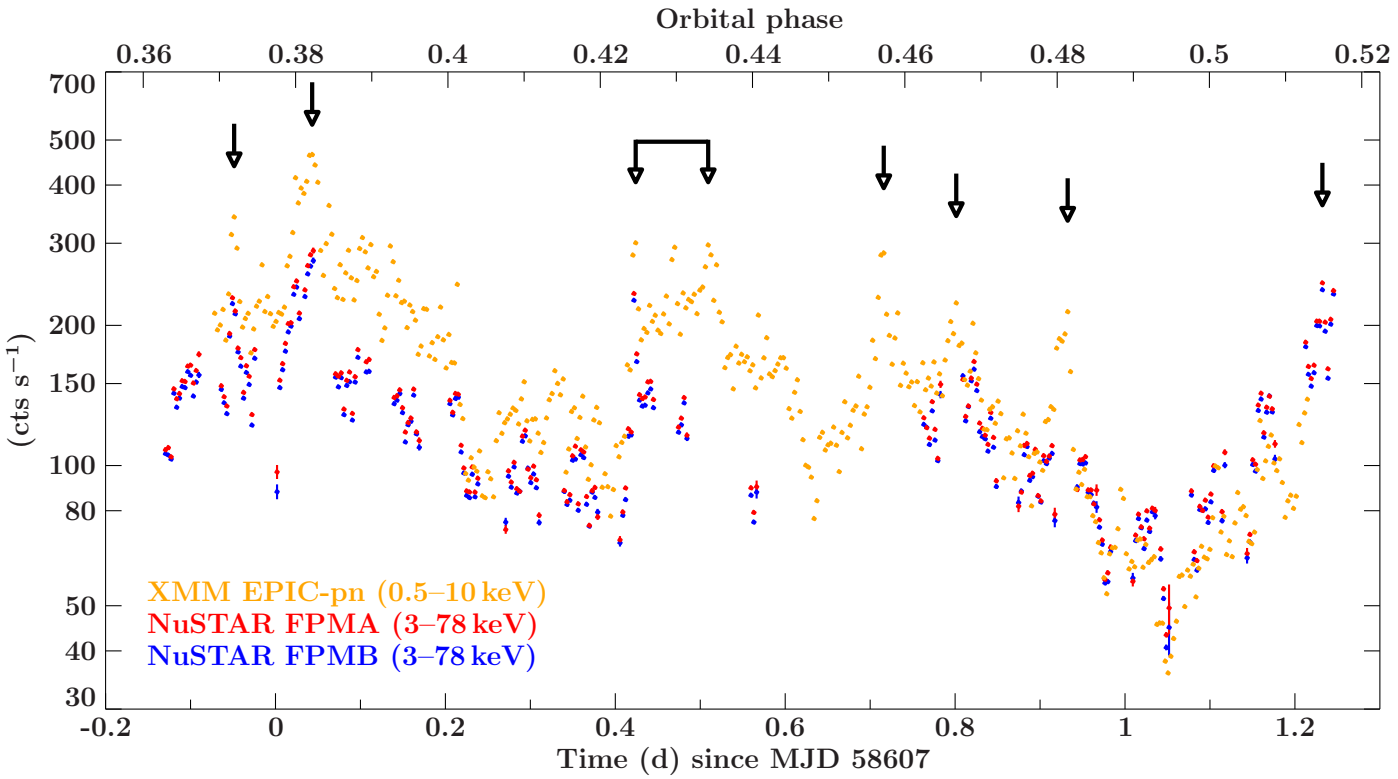

Fig. 2. Light curves for *XMM-Newton* EPIC-pn (orange), *NuSTAR* FPMA (red), and FPMB (blue) with a time resolution of $P = 283.44$ s. The count rate is plotted on the y-axis in logarithmic scale against the orbital phase (top axis) and the time of the observation (bottom axis). Major short flares are indicated by single arrows. The connected arrows at ~58607.42 MJD indicate a flaring episode of ~8 ks.

all hardness ratio starts to increase after $T_{\rm obs} \approx 58607.60$ MJD ($\phi_{\rm orb} \approx 0.44$) until $T_{\rm obs} \approx 58607.93$ MJD ($\phi_{\rm orb} \approx 0.48$) followed by a steeper increasing slope until the end of the observation. This was expected from Diez et al. (2022) as we analysed similar energy bands for the hardness ratio: the 3.0–5.0 keV and 20.0–30.0 keV bands which also correspond to the low-energy and continuum parts of the spectrum, respectively. Finally, in the last panel of Fig. 5, the hardness ratio between the 6.0–8.0 keV and 8.0–10.0 keV bands is constant throughout the whole observation, showing no variation in the continuum as in Diez et al. (2022) and Martínez-Núñez et al. (2014).

In summary, it seems that the spectral shape gradually changes at low energies, which is particularly evident between 0.5 keV and 3.0 keV. This could be associated to changes in the behaviour of the absorbing material while the continuum emission from the neutron star seems to be stable.

Further insights into the role played by wind absorption come from a colour–colour diagram (Fig. 6) that shows a typical 'nose'-like shape that has previously been associated with variable absorption in stellar wind, especially in Cyg X-1 (Nowak et al. 2011; Hirsch et al. 2019; Grinberg et al. 2020; Lai et al. 2022). We further discuss our modelling of the colour–colour diagram and its implications for the wind properties in Sect. 5.1.1. To further explore the behaviour of the source, a spectral analysis of the absorption column density on shorter timescales is necessary.

4. Spectral analysis

4.1. Definition of the spectral model

4.1.1. Continuum shape

As this current *XMM-Newton* EPIC-pn work follows results from simultaneous observations analysed in our previous NuSTAR work, we decided to use the same continuum model for direct comparisons and homogeneous continuity of the work. The final continuum model we obtained is the following and we refer to Diez et al. (2022) for a detailed discussion on how this model was obtained:

$$I(E) = N_{\rm H,2} \times (\mathrm{CF} \times N_{\rm H,1} + (1 - \mathrm{CF})) \times (F(E) \times \mathrm{CRSF}, \mathrm{F} \times \mathrm{CRSF}, \mathrm{H} + \mathrm{FeK}\alpha + 10\,\mathrm{keV}). \quad (1)$$

The parameter $N_{\rm H,2}$ accounts for the absorption column density from the interstellar medium and is fixed to 3.71×10^{21} cm^{-2} using the NASA HEASARC $N_{\rm H}$ tool website[4] (HI4PI Collaboration et al. 2016). The absorption $N_{\rm H,1}$ corresponds to the stellar wind embedding the neutron star and is a free parameter. Those two absorption components are described by the `tbabs` model (Wilms et al. 2000) with the corresponding abundances and cross-sections from Verner et al. (1996).

The covering fraction (CF) quantifies the clumpy structure of the stellar wind and ranges between 0 (the obscurer does not cover the source) and 1 (the obscurer is fully covering the source). This is characteristic of a partial covering model, of which several flavours can be found in the literature (e.g.

[4] https://heasarc.gsfc.nasa.gov/cgi-bin/Tools/w3nh/w3nh.pl

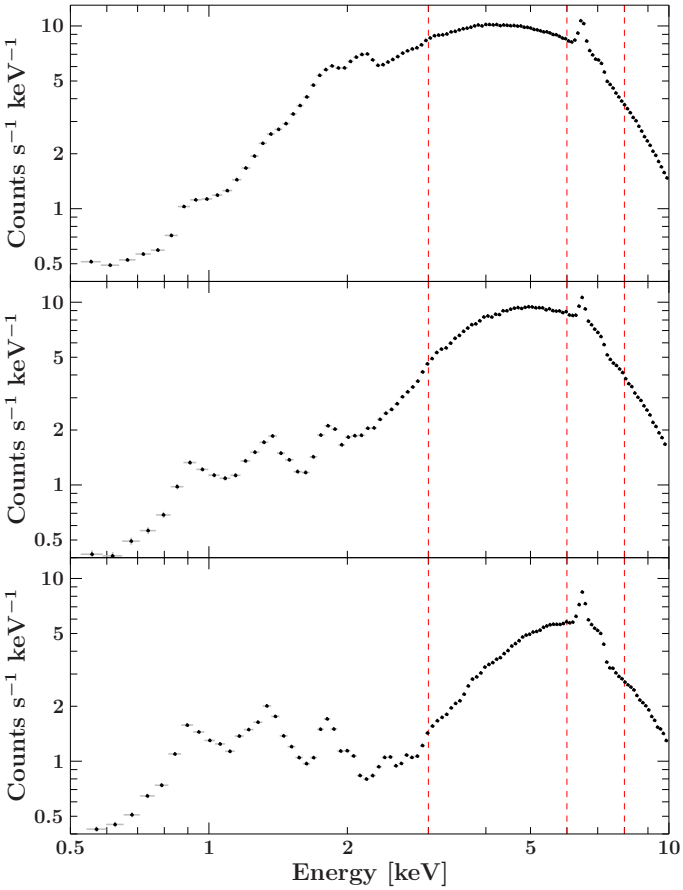

Fig. 3. *XMM-Newton* EPIC-pn spectra extracted during the three different phases of the observation. These are shown in chronological order from the top to the bottom panel: Phase of stable hardness ratio ($0.37 \lesssim \phi_{\rm orb} \lesssim 0.44$), phase of the loss of *NuSTAR* data ($0.44 \lesssim \phi_{\rm orb} \lesssim 0.46$), and phase of the rise of the hardness ratio ($0.46 \lesssim \phi_{\rm orb} \lesssim 0.51$), respectively. The vertical red dashed lines indicate the four energy bands we chose for the extraction of the energy-resolved light curves.

Martínez-Núñez et al. 2014; Fürst et al. 2014a; Malacaria et al. 2016), and was found to provide the best description of the clumpy absorber in Vela X-1.

The function $F(E)$ describes the spectral continuum of the accreting neutron star and is empirically described by a power law with a high-energy cutoff (see e.g. Staubert et al. 2019). Several models from the literature may account for the description of the high-energy cutoff. Our best results were obtained with the `FDcut` high-energy cutoff, whereby

$$F(E) \propto E^{-\Gamma} \times \left(1 + \exp\left(\frac{E - E_{\rm cut}}{E_{\rm fold}}\right)\right)^{-1}, \quad (2)$$

where Γ, $E_{\rm cut}$, and $E_{\rm fold}$ stand for the photon index, the cutoff energy, and the folding energy, respectively.

In the spectrum of Vela X-1, two cyclotron resonant scattering features (CRSFs, or cyclotron lines) are present with a prominent harmonic line at ~55 keV and a weaker fundamental at ~25 keV (Kendziorra et al. 1992; Kretschmar et al. 1997; Orlandini et al. 1998; Kreykenbohm et al. 1999, 2002; Fürst et al. 2014b; Diez et al. 2022). These features are typical of highly magnetised neutron stars and can be observed in the source X-ray spectrum as broad absorption lines. CRSFs result from resonant scattering of photons by electrons in strong magnetic fields from the ground level to higher excited Landau levels followed by radiative decay (see Staubert et al. 2019, for a review). We describe the CRSFs using two multiplicative Gaussian absorption lines with the `gabs` parameter in XSPEC, corresponding to the fundamental and harmonic CRSF, meaning that:

$$\mathrm{CRSF(E)} = \exp\left[-\left(\frac{\mathrm{d}}{\sigma\sqrt{2\pi}}\right)\exp\left(-0.5\left(\frac{\mathrm{E} - \mathrm{E_{cyc}}}{\sigma}\right)^2\right)\right], \quad (3)$$

where d is the line depth and σ the line width.

The fluorescent emission line associated with FeKα is modelled with a narrow Gaussian line component with the `egauss` parameter in XSPEC around 6.4 keV, with width and flux left to vary. The 10 keV feature is described by a broad Gaussian line component in absorption. The physical origin of this feature is still unknown, but in Diez et al. (2022) we discussed the presence of this feature in Vela X-1.

4.1.2. Line emission

Thanks to the low-energy coverage permitted by *XMM-Newton* EPIC-pn and a better resolution than *NuSTAR* between 3 and 10 keV, we now have access to new features that we need to include in our model. In our previous analysis, the fluorescent emission line associated with the FeKβ could not be resolved from the FeKα emission line. This is now possible with the *XMM-Newton* EPIC-pn energy resolution and we model it with a Gaussian component around 7.1 keV, with flux left free to vary but with fixed width.

Particularly in the most absorbed spectra of our observation, we can now also identify multiple emission lines between 0.5 keV and 4 keV (see last panel of Fig 3). The absorption from the stellar wind is very strong towards the end of the observation (i.e. towards late orbital phases; see Diez et al. 2022), and therefore the strong continuum emitted by the neutron star is heavily absorbed and reveals the emission lines normally subsumed in the continuum when the absorption is less strong.

To help us to identify the energy of individual observed features, we based our search on *Chandra*/HETGS results of Amato et al. (2021), who analysed Vela X-1 at orbital phase $\phi_{\rm orb} \approx 0.75$, which is even more affected by the stellar wind (see Fig.1). Because of the limited energy resolution of EPIC-pn, Doppler shifts with orbital phase and triplets or faint lines cannot be resolved in this work. To search for the lines in EPIC-pn spectra, we had to fix the features (such as the CRSFs and the 10 keV feature) and continuum parameters (such as $E_{\rm cut}$ and $E_{\rm fold}$) that are not covered by the EPIC-pn instrument. We fixed them to the average *NuSTAR* values from Diez et al. (2022) for highly absorbed spectra to have an accurate description of the continuum in order to focus on the line description. We performed this search 'by hand', fitting Gaussian components to observed line features in the most absorbed time-resolved spectra of the observation until we obtained a satisfactory reduced chi-square. An example of such a spectrum is shown in Fig.7. The energies of the narrowest lines (Ne x Lyα, Mg xii Si xiv Lyα, S xvi Lyα, Ca ii–xii Kα) have to be fixed to previous studies and their widths to 10^{-6} keV.

A list of the soft lines identified in this work and a comparison with previous studies is shown in Table 2. We note that, here we do not aim to perform an in-depth study of the emission-line variability but rather an absorption study of the stellar wind in Vela X-1. The instrumental issues described in Sect. 2 with the limited energy resolution of EPIC-pn can explain the discrepancies obtained for some lines in comparison with previous work, in particular for O viii Lyα and Ca ii–xii Kα. The Ar vi–ix and Ca ii–xii Kα lines were not detected in Amato et al. (2021).

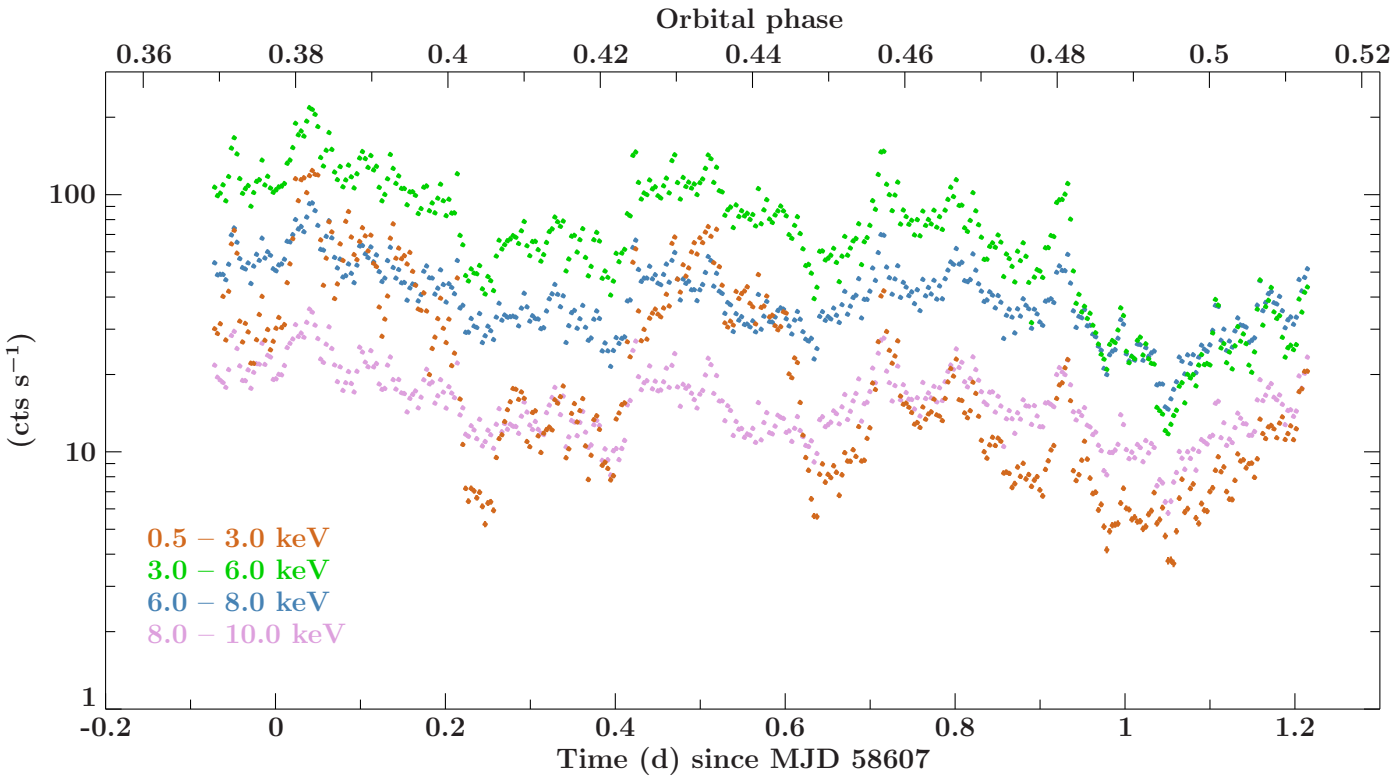

Fig. 4. Light curves for *XMM-Newton* EPIC-pn in different energy bands with a time resolution of $P = 283.44$ s. The count rate shown on the y-axis in logarithmic scale is plotted against the orbital phase and the time of the observation. The energy bands are 0.5–3.0, 3.0–6.0, 6.0–8.0, 8.0–10.0 keV.

However, those lines were identified in Schulz et al. (2002), Goldstein et al. (2004), and Watanabe et al. (2006) for Vela X-1 and in Fürst et al. (2011) for the HMXB GX 301–2. The different charge states of Ca and Ar cannot be resolved, and so in Table 2 we give the potential candidates as in Schulz et al. (2002) and Watanabe et al. (2006).

We also detect a 3.2 keV line that has not been reported in previous work. This feature can most likely be attributed to the S XV RRC, with its ionisation potential of 3.224 keV (Drake 1988). While lower charge states of Ar are present (2.9661 keV), the line energies for both He-like Ar XVII r at 3.140 keV (Drake 1988) and H-like Ar XVIII Lyα at 3.321 keV (Garcia & Mack 1965) are too far away to reasonably match the fitted line energy. The same is true for the H-like S XVI Lyβ and Lyγ lines at 3.106 and 3.276 keV (Garcia & Mack 1965), respectively, even though the S XVI Lyα feature is clearly detected. If this feature were indeed caused by the S XV RRC, we would expect RRC features from the more abundant ions as well. However, at the low resolution of the CCD spectra, many of the other RRC candidates are too blended to allow for a clear detection; for instance, the Si XIII RRC at 2.438 keV (Drake 1988) blends with the S XV Heα complex, the Ne X RRC at 1.362 keV (Garcia & Mack 1965) blends Mg XI Heα, and the O VIII RRC at 0.871 keV (Garcia & Mack 1965) with the Ne IX Heα lines (see e.g. Sako et al. 1999).

Finally, our final and best-fit model, which we use for the time-resolved spectroscopy in this work, is:

$$I(E) = N_{\rm H,2} \times [(\mathrm{CF} \times N_{\rm H,1} + (1 - \mathrm{CF})) \times (F(E) \times \mathrm{CRSF,F} \times \mathrm{CRSF,H}) + \mathrm{FeK}\alpha + \mathrm{FeK}\beta + 10\,\mathrm{keV} + \mathrm{Soft\ lines}]. \quad (4)$$

4.2. NuSTAR-orbit-by-orbit analysis

We can now perform the analysis on shorter timescales with both *XMM-Newton* EPIC-pn and *NuSTAR* to access the variability of the stellar wind at low energies. Combining both datasets — and thus increasing the covered spectral range— limits the impact of possible degeneracy between the power-law slope and absorption strength. *NuSTAR* data are especially crucial at high absorption, when it is especially difficult to constrain the continuum with *XMM-Newton* only.

In Diez et al. (2022), we extracted a spectrum for every orbit of *NuSTAR* around the Earth, which is referred to here as '*NuSTAR*-orbit' for the remainder of the paper. This should not be confused with the duration of a binary orbit of the neutron star around its companion. For the simultaneous *XMM-Newton* EPIC-pn data, we decided to extract a spectrum using the same good time intervals (GTIs) used for the *NuSTAR*-orbit-by-orbit analysis with *NuSTAR* data in order to have a broad X-ray band description of the stellar wind on the same timescale. Due to the different start and stop times of the observations, there are *NuSTAR*-orbits without simultaneous *XMM-Newton* EPIC-pn data (see Fig. 2). Moreover, during the *NuSTAR* campaign, data were lost because of ground-station issues, resulting in no or limited *NuSTAR* coverage for parts of our *XMM-Newton* observation. For the 'missing' *NuSTAR*-orbits, we took the average duration of a *NuSTAR*-orbit, which lasts ~0.067 MJD (~5.8 ks), in order to extract *XMM-Newton* EPIC-pn spectra. Overall, we have 1 *NuSTAR*-orbit covered by *NuSTAR* only, 2 *NuSTAR*-orbits covered by *XMM-Newton* EPIC-pn only, 4 *NuSTAR*-orbits partially covered by one of the two instruments, and 14 *NuSTAR*-orbits fully covered by both instruments (Fig. 8). We fit the data

Table 2. Details of soft emission lines between 0.5 keV and 4 keV.

Line	Detected energy from previous work (keV)	Reference energy (keV)	Identified energy for this work (keV)
O VIII Lyα	$0.6538^{+0.0005}_{-0.0011}$ [a]	0.6541 [c]	$0.6211^{+0.0130}_{-0.0011}$
Ne IX (f, i, r)	$0.90460 \pm 0.00033/0.91454 \pm 0.00034/0.92154 \pm 0.00034$ [b]	0.905/0.915/0.922 [c]	$0.928^{+0.011}_{-0.012}$
Ne X Lyα	$1.02130^{+0.00015}_{-0.00014}$ [b]	1.02196 [d]	1.02130 (fixed)
Mg XI (f, i, r)	$1.3305 \pm 0.0002/1.3426^{+0.0003}_{-0.0002}/1.3517^{+0.0002}_{-0.0003}$ [b]	1.3311/1.3431/1.3522 [c]	$1.338^{+0.012}_{-0.019}$
Mg XII Lyα	1.4720 ± 0.0002 [b]	1.4723 [d]	1.4720 (fixed)
Si XIII (f, i, r)	$1.8388 \pm 0.0002/1.8536 \pm 0.0002/1.8643 \pm 0.0002$ [b]	1.8382/1.8530/1.8648 [e]	$1.823^{+0.014}_{-0.013}$
Si XIV Lyα	2.0049 ± 0.0003 [b]	2.0056 [f]	2.0049 (fixed)
S XV (f, i, r)	$2.4287^{+0.0007}_{-0.0008}/2.4463^{+0.0007}_{-0.0009}/2.4590^{+0.0006}_{-0.0009}$ [b]	2.4291/2.4463/2.4606 [e]	$2.439^{+0.029}_{-0.027}$
S XVI Lyα	$2.6207^{+0.0016}_{-0.0017}$ [b]	2.6196 [f]	2.6207 (fixed)
Ar VI–IX	$2.9661^{+0.0043}_{-0.0099}$ [g]	2.9619 – 2.9675 [h]	2.9661 (fixed)
S XV RRC?		3.224 [c]	$3.23^{+0.04}_{-0.06}$
Ca II–XII Kα	$3.6905^{+0.0022}_{-0.0009}$ [i]	3.6911 – 3.7110 [h]	$3.822^{+0.019}_{-0.102}$

(f, i, r): Referring to forbidden, intercombination, and resonance lines respectively.
(fixed): to previous detected energies.
Note: To convert from Å in previous works to keV, we compute E[keV] = $hc \div \lambda$[Å] where hc = 12.39842 (with values for h, c and e from CODATA 2018, Tiesinga et al. 2021) and round to relevant significant digits.
[a] Lomaeva et al. (2020), [b] Amato et al. (2021), [c] Drake (1988) , [d] Erickson (1977), [e] Hell et al. (2016), [f] Garcia & Mack (1965), [g] Schulz et al. (2002), [h] House (1969), [i] Watanabe et al. (2006)

using the model from Eq. 4, with adaptations as necessitated by the different instrumental coverage as discussed in the following.

Firstly, for the *NuSTAR*-orbits covered by both *NuSTAR* and *XMM-Newton* EPIC-pn, we use a floating cross-normalisation parameter, C_{NuSTAR}, in order to give the relative normalisation between the two *NuSTAR* detectors FPMA and FPMB with the *XMM-Newton* EPIC-pn instrument. The difference between FPMA and FPMB is of the order of ∼2%, and so we can safely assume one normalisation constant to account for both focal plane modules for simplicity.

As discussed in Sect. 2, cross-calibration issues between *NuSTAR* and *XMM-Newton* EPIC-pn are impacting the analysis. To correct the observed up-turn in the *NuSTAR* data at ∼3 keV, we applied two different CFs, CF_{XMM} and CF_{NuSTAR} , for *XMM-Newton* EPIC-pn and *NuSTAR*, respectively. We do not fix CF_{NuSTAR} to previous values from Diez et al. (2022) as this current work benefits from low-energy coverage with *XMM-Newton*, which gives us better constraints on $N_{H,1}$, and therefore on CF_{NuSTAR} , because those two parameters were found to be strongly correlated, as shown in Fig. 7 of Diez et al. (2022). To correct the shift in the FeKα emission line, we apply a gain shift to the *NuSTAR* data in order to align on the iron line energy found with *XMM-Newton* EPIC-pn.

We also introduce another cross-normalisation constant C_{Fe} to account for the flux difference observed in *NuSTAR* relative to *XMM-Newton* EPIC-pn in the emission lines that are covered by both observatories: FeKα and FeKβ. We fix the soft-emission-line energies and widths to the values estimated when analysing the *XMM-Newton* EPIC-pn spectrum at high absorption (see Table 2) as they are not expected to change significantly with time, even if the source is highly variable (Grinberg et al. 2017). The fluxes of the emission lines are left free as their prominence changes depending on the local absorption.

We fix the CRSF parameters and the energy of the 10 keV feature to the values of their corresponding *NuSTAR*-orbit —which we obtained in our previous analysis in Diez et al. (2022)— to help to constrain the low-energy part of the continuum. Degeneracies between $E_{CRSF,F}$ and E_{cut} are expected due to their proximity as seen in Diez et al. (2022); therefore, we also fix the cutoff energy in the same way.

Secondly, for the two *NuSTAR*-orbits only covered by *XMM-Newton* EPIC-pn (*NuSTAR*-orbits number 12 and 13), we fix the CRSFs parameters, the energy of the 10 keV feature $E_{10\,keV}$, and the cutoff energy E_{cut} to the closest *NuSTAR*-orbit values. These parameters cannot be ignored during the fitting because they modify the shape of the broadband continuum, and therefore fixing them to the values of the closest *NuSTAR*-orbit is the most accurate and meaningful solution. We do not use C_{NuSTAR}, gain shift, CF_{NuSTAR}, or C_{Fe} as there is no need to correct for cross-calibration because no coverage from *NuSTAR* is available for those *NuSTAR*-orbits.

Thirdly, for the *NuSTAR*-orbit that is covered by *NuSTAR* only (*NuSTAR*-orbit number 1), the multiple soft emission lines and the FeKβ line identified with *XMM-Newton* EPIC-pn are not resolved by *NuSTAR* alone. However, those emission lines do not impact the shape of the overall continuum of Vela X-1, and therefore they can be safely ignored for fitting the data for simplicity. We tried to fix them to the values of the closest following *NuSTAR*-orbit but no significant difference could be highlighted when comparing the residuals.

We present the results of the *NuSTAR*-orbit-by-orbit analysis in Fig. 8, focusing on the parameters of interest. An example of a fitted spectrum extracted during one *NuSTAR*-orbit with both *XMM-Newton* EPIC-pn and *NuSTAR* is given in Fig. A.4. However, we caution that the different instrumental coverage of individual spectra may result in artificial parameter behaviour, such as outliers.

Discrepancies between *NuSTAR* and *XMM-Newton* EPIC-pn are visible in the cross-normalisation parameter C_{NuSTAR} , reaching ∼20% (not considering outliers), which can be explained by the low-energy up-turn in *NuSTAR* (see Fig. A.4). Moreover, the average energy gainshift of *NuSTAR* relative to *XMM-Newton* EPIC-pn is of -87 eV. This particularly impacts the iron line region as it is covered by both instruments. Therefore, the energy of the iron line shown in the third panel of Fig. 8 is given with respect to the *XMM-Newton* EPIC-pn values, and

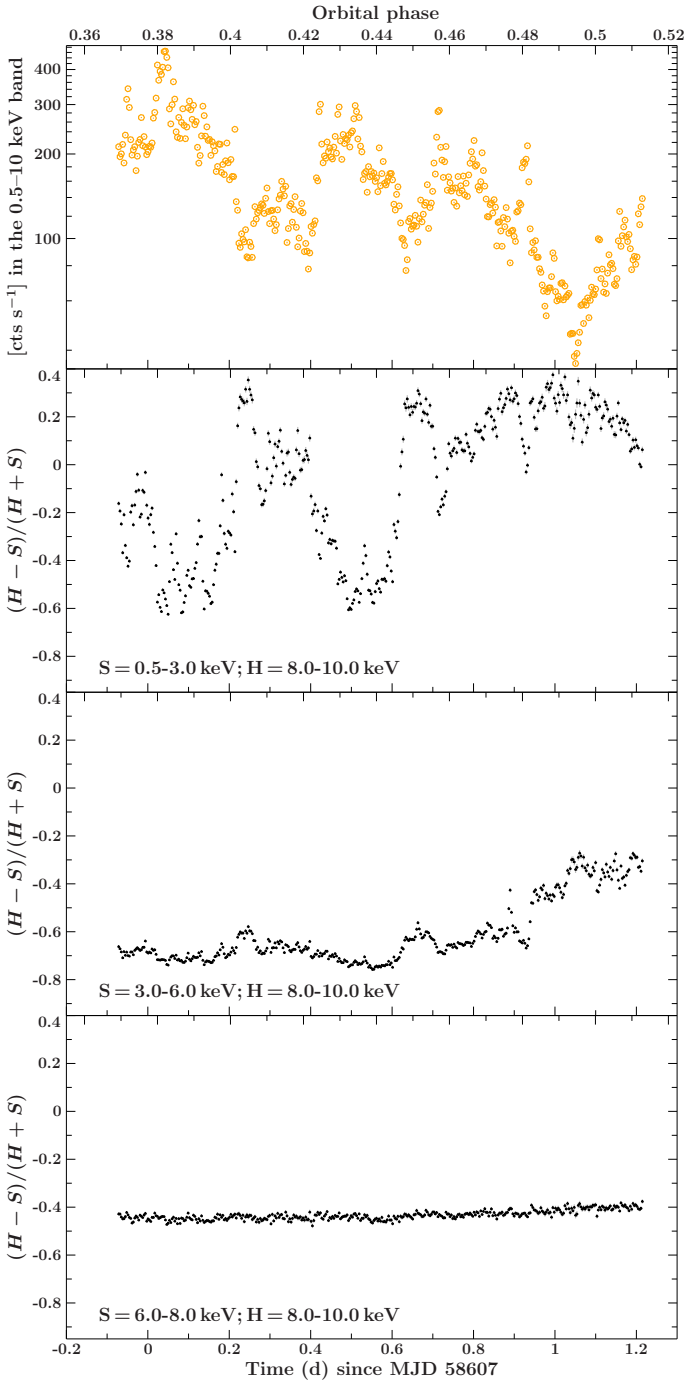

Fig. 5. Light curve and hardness ratios for *XMM-Newton* EPIC-pn. The first panel shows the overall count rate in the 0.5–10 keV energy band as in Fig. 2. The following panels show the hardness ratios between the mentioned energy bands. The time resolution is P = 283.44 s.

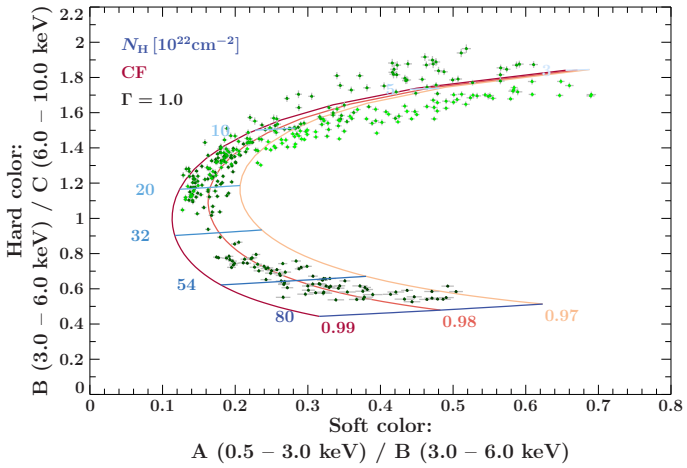

Fig. 6. *XMM-Newton* EPIC-pn colour-colour diagram. The data points represent the ratios of the light curves in hard colour depending on soft colour, from beginning (light green) to end (dark green) of the observation. We also show the theoretical expectation for different covering fractions CF (shades of red, varying from 0.97 to 0.99) and absorption column densities $N_{H,1}$ (shades of blue, varying from 3×10^{22} cm^{-2} to 80×10^{22} cm^{-2}) using our partial covering model from Eq. 4. We used a photon index Γ of 1.0. More details about the simulation and its interpretation are given in Sect. 5.1.1.

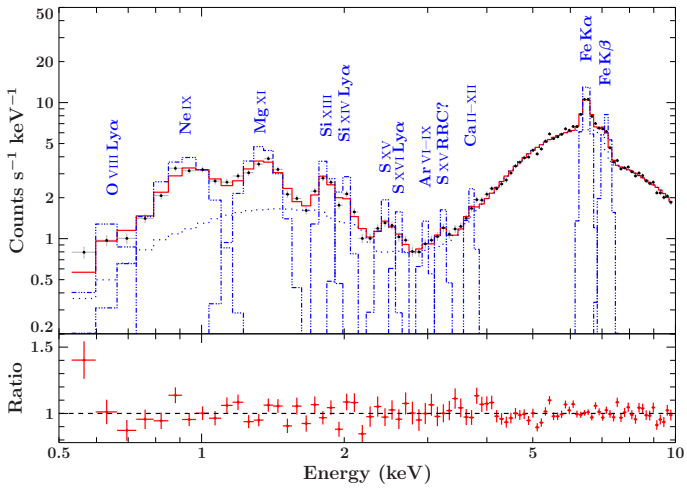

Fig. 7. Example *XMM-Newton* EPIC-pn spectrum (black datapoints). We show the last and most absorbed *NuSTAR*-orbit of our observation. We indicate the individual model components including all lines detected in this dataset (blue dot-dashed Gaussians) and the absorbed continuum (blue dotted line). We refer to Sect. 4.2 for a detailed description of the model and to Table 2 for the soft lines.

the gainshift has to be added to retrieve the *NuSTAR* values, with the exception of the magenta triangle outlier of *NuSTAR*-orbit 1, which is only covered by *NuSTAR*.

Significant variability can be observed in the presented parameters. In particular, $N_{H,1}$ increases by a factor of 6 between the beginning and the end of the observation, showing a very clear rise of the stellar-wind absorption at $\phi_{orb} \approx 0.44 - 0.49$. The energy of the iron line remains relatively stable around ~6.48 keV, but shows local minima, which seem to be anti-correlated with the flux in the 3–10 keV energy band. This anti-correlation with flux appears to be similar for the photon index, which also shows local dips during flares. The photon index varies overall between 0.8 and 1.2, the change of spectral shape being associated with changes in absorption density in the stellar wind and possible degeneracy with the amount of absorption. We discuss the details of these relationships and a further investigation of them in Sect. 5.

While the CF with *XMM-Newton* EPIC-pn CF_{XMM} remains very stable around 0.98, the CF with *NuSTAR* is much more variable, ranging between 0.3 and 0.98 (we note the different y-axis range compared to CF_{XMM}) as in Diez et al. (2022) when analysing *NuSTAR* data alone. This is due to the up-turn in *NuSTAR* data at low energies (see Fig. A.4). We discuss tests per-

formed to assess some possible sources of this effect in Sect. A.3, and in particular a possible contribution from dust scattering. We are unable to find a plausible physical explanation and therefore conclude that the problem is due to some remaining calibration effects. In Diez et al. (2022), we discussed the problems encountered with the low-energy effective area correction for FPMA (Madsen et al. 2020) in our observation. While these problems should not affect FPMB, together with the high variability of the CF as deducted from the *NuSTAR* data alone, they imply a reduced reliability of the *NuSTAR* data for our observation in this energy range. Moreover, looking at Fig. 6, it is obvious that a CF of less than 0.97 would not describe the data. We therefore decide to focus our discussion on *XMM-Newton*-driven CF values for the remainder of the paper.

4.3. Pulse-by-pulse: XMM-Newton only

The sensitivity of *XMM-Newton* EPIC-pn allows us to extract a spectrum down to the pulse period of the neutron star (283 s). We performed a spectral analysis for every pulse of the neutron star to explore further variability on shorter timescales.

Given the cross-instrumental issues between *XMM-Newton* and *NuSTAR* and the different coverage of the overall observation (due to both LEO of *NuSTAR* and the loss of data), this analysis is performed on *XMM-Newton* data only. While for the *NuSTAR*-orbit-by-orbit analysis it was still possible to safely determine the individual contribution of each instrument for each GTI and exclude outliers when needed, such an approach is not feasible for the pulse-by-pulse analysis. The pulse-by-pulse results for this observation with *NuSTAR* only are presented in Diez et al. (2022).

We again use the model from Eq. 4, setting up the initial parameters for each pulse spectrum from the results of the corresponding *NuSTAR*-orbit of the *NuSTAR*-orbit-by-orbit spectral analysis. Given the low signal of the individual datasets, we fix all parameters but the photon index Γ, the covering fraction CF_{XMM}, the absorption column density from the stellar wind $N_{\mathrm{H,1}}$, the energy of the fluorescent FeKα line, and the flux of all the emission lines.

In Fig. 9, we present the results of the pulse-by-pulse analysis for the *XMM-Newton* EPIC-pn data. The typical reduced chi-square χ^2_{red} of the fittings is ∼1.20 and the time resolution of ∼283 s gives us access to much more parameter variability along the orbital phase than in Fig. 8. Again, the rise of the absorption column density $N_{\mathrm{H,1}}$ is clearly visible but with much more local instability, such as two local episodes of high absorption at orbital phases ∼0.40 and ∼0.44. The overall track is very similar to the hardness ratio between the 3–6 keV and 8–10 keV energy bands shown in the third panel of Fig. 5 and is even more amplified on the second panel of the same figure for the hardness ratio between the softest and hardest energy bands. This is expected as mainly low-energy photons are absorbed by the stellar wind, and therefore the underlying spectral shape becomes harder during those high-absorption episodes, as explained in Sect. 3. On the other hand, episodes of low absorption seem to be associated with flaring periods according to Fig. 9, which could be explained by accretion of clumps on the line of sight of the observer, as described in Diez et al. (2022). In Diez et al. (2022), we observed a correlation between CF_{NuSTAR} and $N_{\mathrm{H,1}}$, but also with flux. However, there does not seem to be any correlation between *XMM-Newton*-driven CF values and $N_{\mathrm{H,1}}$ or flux $\mathcal{F}$ for this work. The photon index Γ is relatively variable, particularly towards the end of the observation. This should be taken with caution as the error bars get larger and the absorption is so strong that there may be some degeneracy between $N_{\mathrm{H,1}}$ and Γ .

5. Discussion: The variable absorber

5.1. Evolution of absorption along the binary orbital phase: the onset of wakes

The main finding of our paper is the detailed analysis of the rise of the $N_{\mathrm{H,1}}$ value and therefore of the absorption in the stellar wind, which we interpret as the onset of the wakes. This is the first time this orbital period and the corresponding wind structure are probed in a time-resolved way with a modern X-ray instrument (see Fig. 5 in Kretschmar et al. 2021).

5.1.1. X-ray colour evolution with orbital phase

We observe an interesting gradual increase in the hardness ratio between the 3.0–6.0 keV and 8.0–10.0 keV energy bands (see third panel of Fig. 5). This is more a consequence of a general geometric change in the stellar wind than of the local accretion of clumps. When the wakes are coming through our line of sight (see Fig. 1), the absorption in the stellar wind increases, preferentially absorbing low-energy photons emitted in the vicinity of the neutron star starting from $\phi_{\mathrm{orb}} \approx 0.44$. In our pulse-by-pulse analysis, this rise in the absorption column density $N_{\mathrm{H,1}}$ can be directly measured from Fig. 9.

On the other hand, the hardness ratio of high-energy bands is constant (last panel of Fig. 5), implying a stable behaviour of the continuum emission from the neutron star. Martínez-Núñez et al. (2014) observed similar behaviour —spectral changes at low energies due to increasing absorption but stable overall source continuum— during their observation, which covered eclipse egress and a major flare.

The above is supported by the behaviour of the source on the colour–colour diagram (Sect. 3.3) where it describes a nose shape (Fig. 6). This is typical of the presence of a partial coverer with variable column density in the system (e.g. Hirsch et al. 2019; Grinberg et al. 2020, in Cyg X-1). As would be expected given the onset of the wake, the source evolves along the track with time, as indicated by transition from light (early in the observation) to dark green (late in the observation) data points in the figure.

Figure 10 shows how absorption impacts the observed spectrum modelled by Eq. 4, which consists of a power-law continuum with a high-energy cutoff, assuming a certain CF. In the case of a continuum fully covered by the obscurer (CF = 1, dashed lines), the flux ratios in the soft colour (A/B) and in the hard colour (B/C) decrease as $N_{\mathrm{H,1}}$ grows, leading to a positive correlation between those ratios for the covered spectrum. On the other hand, if we consider a spectrum where this time only a certain fraction CF < 1 of the continuum is absorbed by the stellar wind (solid lines), the flux in the A band will remain constant as $N_{\mathrm{H,1}}$ grows after a certain threshold. In the example of a covering fraction of 0.9, this happens at $N_{\mathrm{H,1}} = 54 \times 10^{22}\,\mathrm{cm}^{-2}$ according to expectations from Fig. 10. Simultaneously, the fluxes in the B and C bands continue to decrease together as $N_{\mathrm{H,1}}$ grows. Hence, the softer colour becomes softer as the harder colour does not change, leading to the observed nose-shape colour–colour diagram in Fig. 6. This probes the necessity of a partial covering model to describe the data. A higher CF leads to a less elongated curve.

We use an averaged Γ over the values obtained in Fig. 8 for our observation. We simulate a grid of colour–colour tracks for

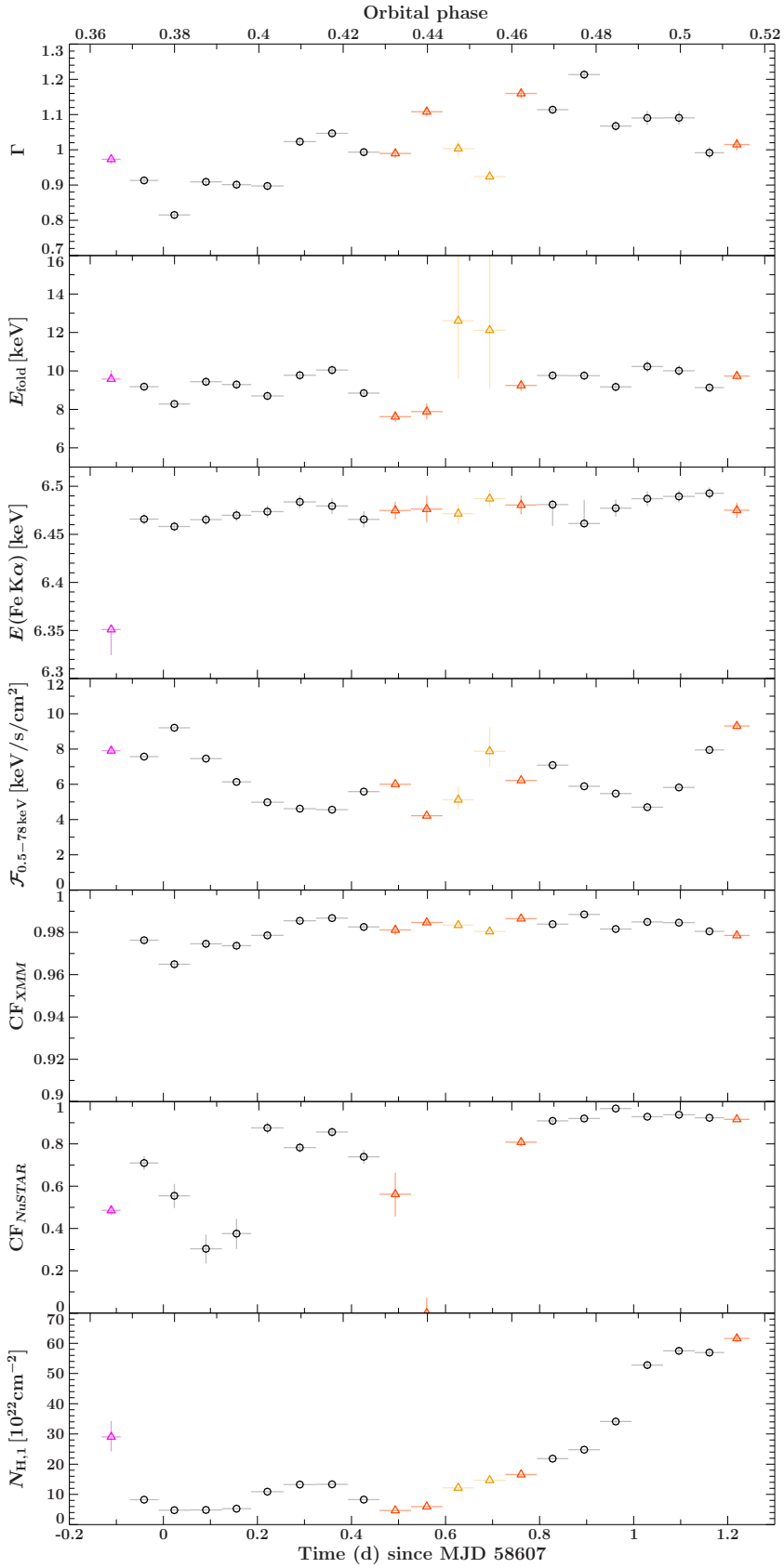

Fig. 8. Results of the *NuSTAR*-orbit-by-orbit analysis with *NuSTAR* and *XMM-Newton* as a function of time, together with the corresponding binary orbital phase. From top to bottom: Photon index (Γ), folding energy ($E_{\rm fold}$) in keV, energy of the FeKα line in keV, unabsorbed flux $\mathcal{F}_{0.5-78\ \rm keV}$ in keV s^{-1} cm^{-2}, CFs with *NuSTAR* (CF$_{NuSTAR}$) and *XMM-Newton* EPIC-pn (CF$_{XMM}$), absorption from the stellar wind $N_{\rm H,1}$ in 10^{22} cm^{-2}. Circles show data fully covered by both *XMM-Newton* EPIC-pn and *NuSTAR*. Triangles show data missing coverage from one of the two instruments. Magenta marks the data only covered by *NuSTAR* (*NuSTAR*-orbit 1) and orange the data fully covered by one instrument but partially by the second one (*NuSTAR*-orbits 10, 11, 14 and 21). Finally, yellow is used to denote data only covered by *XMM-Newton* EPIC-pn (*NuSTAR*-orbits 12 and 13).

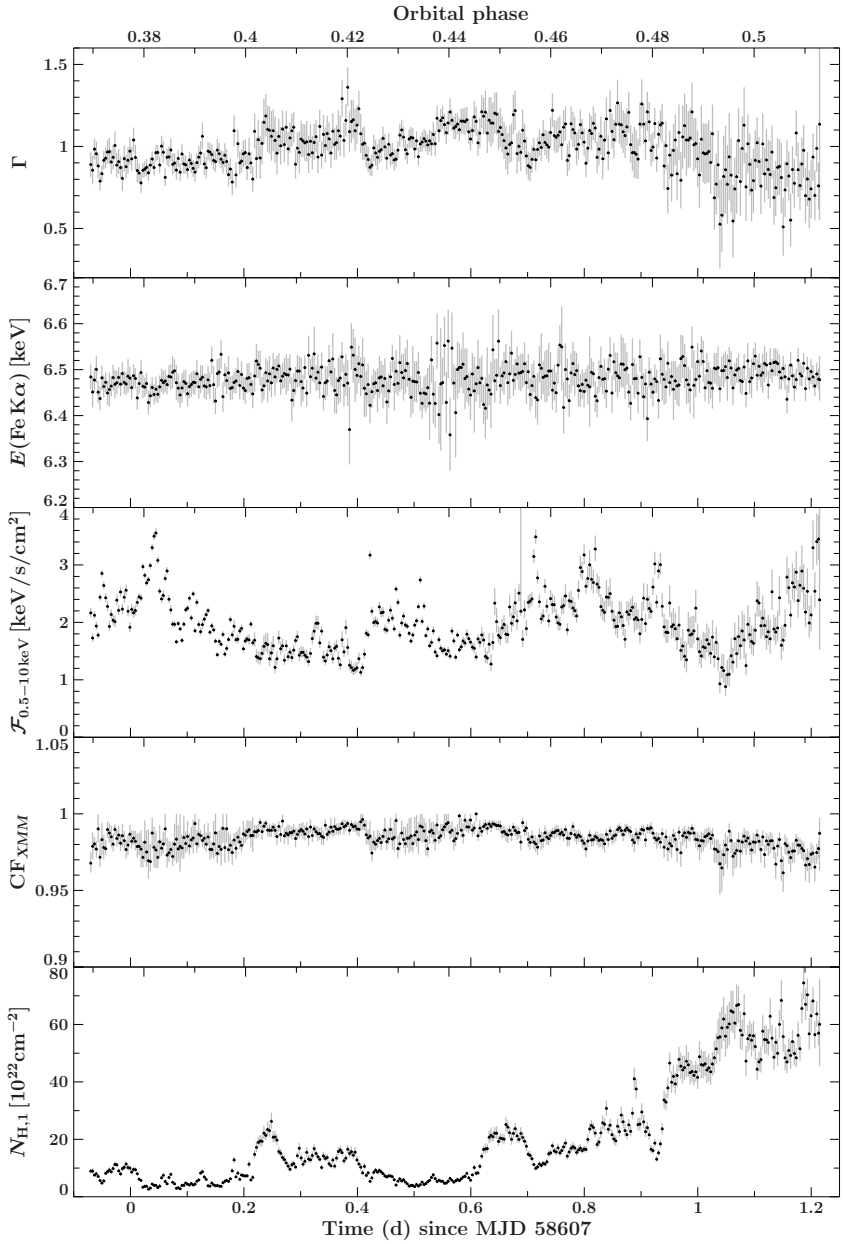

Fig. 9. Results of the pulse-by-pulse analysis as a function of time, together with the corresponding binary orbital phase. The panels show (from top to bottom) photon index (Γ), energy of the FeKα line in keV, unabsorbed flux $\mathcal{F}_{0.5-10\,\mathrm{keV}}$ in keV s^{-1} cm^{-2}, CF with *XMM-Newton* EPIC-pn (CF$_{XMM}$), and absorption from the stellar wind $N_{\mathrm{H,1}}$ in 10^{22} cm^{-2}.

varying values of N_{H} and covering fraction and include the results in Fig. 6. Data and simulations agree very well, supporting our interpretation.

5.1.2. Comparison with previous observations and model descriptions

While absorption values have been determined by many authors with various different satellites (see Kretschmar et al. 2021, for an overview), there are few data sets that cover a significant range in orbital phase within an individual binary orbit and therefore that do not mix potential binary orbit-to-orbit variations in wake structures. After correcting for differences in orbital phase definitions in the original papers, in Fig. 11 we compare the absorption values we derived with data points from Ohashi et al. (1984) and Haberl & White (1990). Different spectral models used to fit spectra and to derive N_{H} may introduce systematic shifts in the obtained values. Still, the data taken over many years appear to cover a similar range, but sometimes with quite different values at the same orbital phase, as seen already in Kretschmar et al. (2021), indicating that the structures causing these variations are not stable in orbital phase. On the other hand, the duration of the overall rising trend from low absorption to a highly absorbed 'plateau' is rather similar in slope —N_{H} values double over a time range of 0.02 in orbital phase or ∼15.4 ks— suggesting that similar larger structures in the wind exist, which may differ somewhat in their relative orientation.

In Fig. 12, we compare our derived N_{H} values with some of the few examples of column densities derived from hydrodynamical model calculations. However, it is important to note that these models start from quite different assumptions (see also Table 3) and were not made for direct comparison. First of all, the

Table 3. Parameters used in the model curves shown in Fig. 12. All the simulations use circular binary orbits with a fixed distance of the neutron star from the stellar surface. The last row shows parameter ranges found by more recent studies of the Vela X-1 system (since the year 2000), as compiled by Kretschmar et al. (2021).

System discussed	Donor star mass ($M_\odot$)	Donor star radius ($R_\odot$)	Stellar wind mass loss ($M_\odot$ yr^{-1})	Stellar wind v_{esc} (km s^{-1})	Neutron star M_X ($M_\odot$)	Neutron star distance ($R_\star$)	Ref. and Notes
Generic HMXB	22	35.2	5.8×10^{-6}	1300	1.4	1.59	[B91]
Vela X-1	23.1	30	4×10^{-6}	1400	1.86	1.77	[MW15b]
EXO 1722−363	15	29	1×10^{-6}	500	1.9	1.75	[MWB12]
Vela X-1	21–28	27–32	$0.4–2 \times 10^{-6}$	380–750	1.8–2.1	1.56–2	[K21]

[B91] Blondin et al. (1991). Showing the 'full simulation', Fig. 8 in the publication.
[MW15b] Manousakis & Walter (2015b). Stellar parameters from Manousakis & Walter (2015a).
[MWB12] Manousakis et al. (2012)
[K21] Kretschmar et al. (2021). Distance variation from eccentricity,'; the binary orbit is very well known.

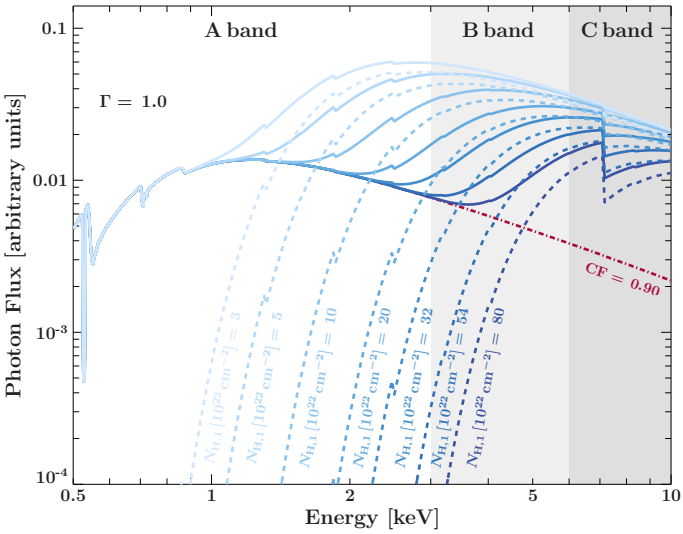

Fig. 10. Effect of increasing absorption on our model from Eq. 4 with photon index $\Gamma = 1.0$ and without emission lines to focus on the evolution of the continuum shape. We assume a CF of 0.9 and a varying absorption column density $N_{H,1}$ from 3×10^{22} cm^{-2} to 80×10^{22} cm^{-2} covering the range obtained in Fig. 9. The shaded grey areas indicate three energy bands of interest: The A band from 0.5 to 3 keV, B band from 3 to 6 keV, and C band from 6 to 10 keV. The resulting observed spectrum (solid lines) is the sum of the spectrum not covered by the stellar wind (dash-dotted line) and the covered spectrum (dashed lines). See Fig. 3 of Diez et al. (2022) for an illustrated picture of the partial covering model.

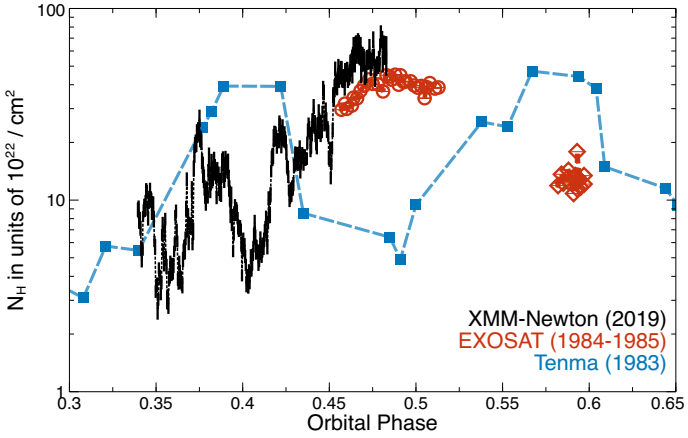

Fig. 11. Comparison of the N_H values determined in this study with historical measurements taken during individual binary orbits by *Tenma* (Ohashi et al. 1984) and *EXOSAT* (Haberl & White 1990). We highlight the overall similar slope of the different rising curves. See text for details.

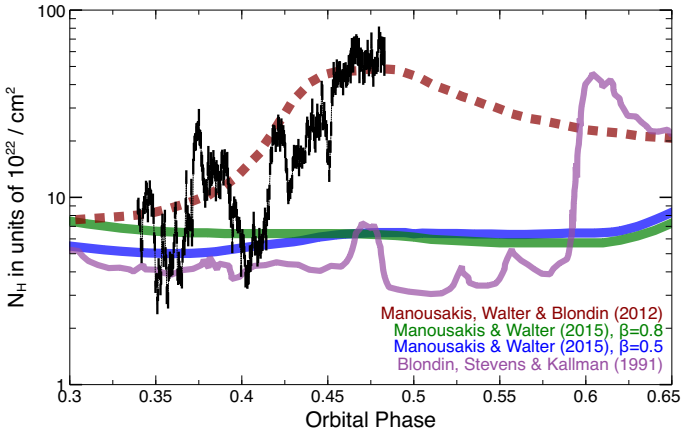

Fig. 12. Comparison of the N_H values determined in this study with a range of model results for N_H from hydrodynamic simulations for Vela X-1 or similar, but not identical model systems. See the main text and Table 3.

curves shown for the models of Manousakis & Walter (2015b) and Manousakis et al. (2012) are time-averaged values of column density over orbital phase, smoothing out the expected significant N_H variability from binary orbit to binary orbit, while the result from Blondin et al. (1991) is taken from the simulation of a single binary orbit in a model including a tidal stream. It is evident that neither this last model nor the relatively low and little varying average column density predicted by Manousakis & Walter (2015b) shows a marked rise at early orbital phases as found in the data. One of the reasons for this may be the rather high wind velocities and mass-loss rates assumed in these studies, and certainly found in earlier studies of Vela X-1, while more modern studies assume lower wind velocities (see Table 7 and Fig. 19 in Kretschmar et al. 2021). The visually best matching curve from Manousakis et al. (2012) was, on the other hand, calculated for a different system, EXO 1722−363, albeit with relatively similar system parameters to Vela X-1, and assuming a relatively slow wind. Updated hydrodynamical simulations accounting for the current best knowledge of orbital and wind parameters of the system, and taking the non-negligible eccentricity into account, would be very welcome.

5.2. Origin and nature of the absorber

The continuum from the neutron star dominates the emission in the spectrum of Vela X-1 until $\phi_{\rm orb} \approx 0.44$. At this orbital phase, the absorption column density increases together with the strength of soft emission lines between 0.5 and 4 keV. Figure 13 shows the evolution of the flux of some lines with time. In particular, we can see the fluxes of the Ne IX and S XV are mostly consistent with 0 at the beginning of the observation but start to increase towards the end, revealing the corresponding elements in the spectrum of Vela X-1. The presence of strong lines during heavy absorption from the stellar wind suggests that the absorber is localised and the lines originate from a larger scale in the system, as in Watanabe et al. (2006). If these lines originated from the local absorber or close to the vicinity of the neutron star, they would be completely absorbed by the stellar wind and would not appear in the resultant spectrum. Another argument in the favour of this statement is that those soft emission lines are also present in the spectrum of Vela X-1 during the eclipse (Sako et al. 1999), which is when the neutron star and its local absorber are outside the line of sight of the observer.

In Fig. 13, the fluxes of the fluorescent FeKα and FeKβ lines are positive throughout the whole observation, meaning that those lines are visible at all observed orbital phases here and therefore also originate from a larger scale in the system. The situation is less evident for the fluorescent Ca II–XII Kα line, which was more difficult to constrain because of blending with neighbouring lines.

The Ne IX, Mg XI, Si XIII, and S XV complexes are evidence of ionisation of the absorber in the system, as those ions only have two remaining electrons on their orbital. Furthermore, the presence of O VIII, Ne X, Mg XII, Si XIV, and S XVI Lyα lines also indicates ionisation in the system as they are emitted when the last atomic electron transitions from an $n = 2$ orbital to the ground state. According to Amato et al. (2021), the warm photoionised wind of the companion star and smaller cooler regions or clumps of gas can explain the simultaneous contribution of H- and He-like emission lines and fluorescent lines of near-neutral ions. Comparing *Chandra*/HETGS data of Vela X-1 with simulations of propagation of X-ray photons in a smooth and undisturbed wind, Watanabe et al. (2006) stated that fluorescent lines originate from reflection of the stellar photosphere in the extended stellar wind or simply from the accretion wake. Additionally, these authors observed brighter soft emission lines at $\phi_{\rm orb} = 0.5$ than during the eclipse. This indicates a higher production of X-ray line emission caused by highly ionised ions in a region between the neutron star and its massive stellar companion, which is occulted during eclipse. However, this is difficult to confirm with our data and further studies at higher spectral resolution are necessary.

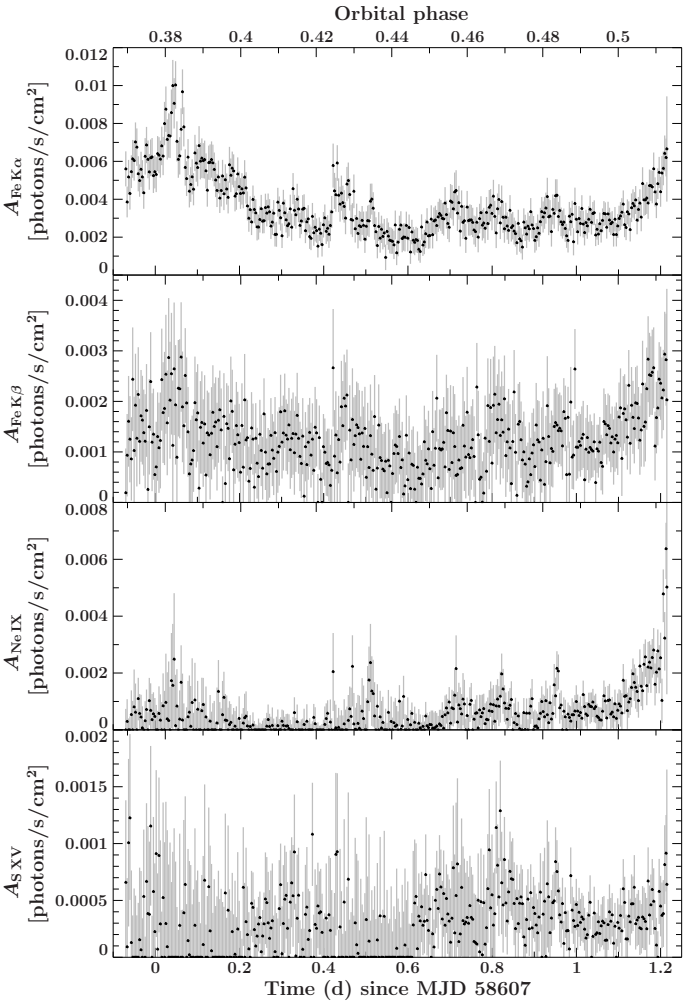

Fig. 13. Fluxes in photons/s/cm^2 of some soft lines obtained within the pulse-by-pulse analysis as functions of time, together with the corresponding binary orbital phase. The panels show (from top to bottom) the flux of the FeKα, the FeKβ, the Ne IX, and the S XV line.

5.3. Short-term absorption variability

5.3.1. Search for characteristic timescales in absorption variability

Theoretical predictions show that variability in a clumpy material can result in typical variability timescales that will depend on the properties of the structures in the stellar wind and/or in the tidal streams in correlation with the orbital parameters of the system (El Mellah et al. 2020). In this section, we therefore present a search for possible indications of such a timescale. To perform this analysis, we used the *Stingray: A Modern Python Library for Spectral Timing* (Bachetti et al. 2022; Huppenkothen et al. 2019; Huppenkothen et al. 2019) Python library. Our pseudo-light curve of $N_{\rm H}$ contains 392 bins with a binning size equal to the pulse period of the neutron star (~283 s). We used different techniques implemented in Stingray, which are:

- Average power spectrum using Leahy normalisation and dividing our data into 11 subsets. This technique allows the search for periodicities in the frequency range between 0.0002 and 0.00175 Hz (see panel (a) of Fig. 14).
- z-search and chi-search techniques to search for periodicity in the frequency range between 0.006 and 0.0033 (see panels (b) and (c) of Fig. 14 respectively).

Neither of the techniques detects a significant periodic or quasi-periodic signal in the evolution of $N_{\rm H}$ in the range of frequencies accessible with our data. The simulations of El Mellah et al. (2020) predict a clear signal in the autocorrelation function equivalent to a cutoff in the power spectrum. Given the quality of our data, the presence of such a feature cannot be assessed. Still, the spectrum presented above is, to our knowledge, the first absorption power spectrum calculated for Vela X-1 in an attempt to obtain such timescales.

To expand the frequency search range to larger values, we also performed a Lomb-Scargle periodogram using the routine

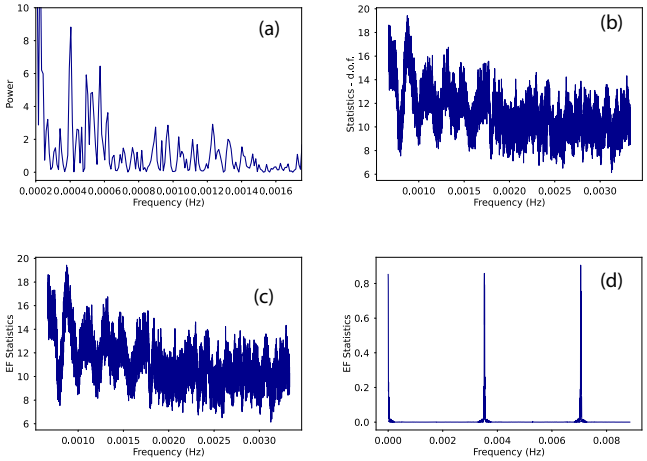

Fig. 14. Timing analysis of $N_{\rm H}$ evolution: (a) Stingray average power spectrum; (b) Stingray z-square function; (c) Stingray chi-square function; (d) Astropy v5.1 Lomb-Scargle Periodogram.

of Astropy v5.1 Timeseries software (Astropy Collaboration et al. 2022) (see panel (d) of Fig. 14). This technique only finds the binning size of our database (and following harmonics) as a possible period but no other periodicity could be found. It does not allow the shape of the power spectrum to be assessed. This search could be enhanced with an extended sample of the $N_{\rm H}$ along one or more binary orbits.

5.3.2. Absorption during flares

During the first two flaring episodes at $\phi_{\rm orb} \approx 0.38$ and $\phi_{\rm orb} \approx 0.43$, we saw in the second panel of Fig. 5 that the hardness ratio between the continuum band and the softest band decreases dramatically, indicating a softening of the underlying spectrum. This is also confirmed in Fig. 8 with the local decreases in photon index during flaring episodes. Therefore, more low-energy photons are detected compared to before the flaring episodes. If more low-energy photons reach the detector plane, this suggests that there is less material on the line of sight of the observer (otherwise they would have been absorbed by the wind), and therefore less absorption from the stellar wind. This is confirmed by our time-resolved spectral analysis in Fig. 8 and in Fig. 9, where the absorption column density of the stellar wind $N_{\rm H,1}$ reaches its minimum during those two flaring episodes.

This is also visible during later short flares with strong but brief softening of the spectral shape together with local minima of $N_{\rm H,1}$ and CF. These short-timescale events could be associated with the accretion of clumps in the vicinity of the neutron star, as already suggested in Martínez-Núñez et al. (2014) and Diez et al. (2022) for Vela X-1. As material falls onto the surface of the neutron star through the accretion column, photons are produced through bremsstrahlung and cyclotron emission. Those photons are then up-scattered through inverse Compton and more X-rays are produced. The more material falls into the neutron star, the more the temperature increases, favouring interactions and X-ray production. Clumps just passing in front of the source on the line of sight of the observer could explain the local maxima in $N_{\rm H,1}$ that are not happening simultaneously with flux changes.

6. Summary and outlook

We analysed simultaneous *XMM-Newton* and *NuSTAR* data of Vela X-1 covering a broad X-ray range at orbital phase ~0.36–0.52. For the spectral modelling, we used our partial covering model first described in Diez et al. (2022). Thanks to the hard X-ray coverage permitted by *NuSTAR* and our results from previous work, we were able to constrain the continuum in order to focus on the absorption variability at lower energies with *XMM-Newton* EPIC-pn for this work.

This is the first time that such a high-time-resolution absorption study of Vela X-1 has been carried out on a broad X-ray range from 0.5 to 78 keV. We traced the onset of the wakes, which are characterised by a rise in the absorption column density $N_{\rm H,1}$ starting at orbital phase ~0.44 as well as local absorption variability due to the accretion of clumps. The slope of the $N_{\rm H,1}$ rise is comparable, and is similar to previous observations, albeit with an orbital-phase lag indicating similar large-scale structures in the wind but with different orientation at different times of observation. We also compared our data with simulations from previous works in the literature but no strong match between observations and theoretical models could be found. This reflects the necessity for further and updated hydrodynamical simulations that account for the latest orbital parameter values (for example: eccentricity > 0) and the complexity of the wind parameters (such as wind velocities and mass-loss rates).

Through high-resolution spectroscopy of the multiple fluorescent lines present in Vela X-1, we performed X-ray photography of the material in the system. The evidence of those lines at different absorption phases suggests sources of emission from local absorber to large-scale structures. This analysis also reveals strong photoionisation of the wind with the presence of highly ionised elements such as Lyα lines of O, Ne, Mg, Si, and S. However, these results have to be considered with caution as the *XMM-Newton* EPIC-pn energy resolution is not sufficient to perform an accurate spectral analysis of individual lines and blending with neighbouring elements can happen. This aspect is beyond the scope of this paper and the analysis of simultaneous *XMM-Newton* RGS data in a future work is needed to disentangle this. Moreover, we used a neutral absorber to describe the absorption from the wind, but the use of `warmabs`[5] for warm absorbers and photoionised emitters would be better suited, as would a higher resolution instrument (such as *Chandra*/HETGS). The upcoming *XRISM* and *Athena* (Barret et al. 2020) are of utmost importance for such a study, as high-resolution spectral analysis is one of their main science goals (XRISM Science Team 2020).

Acknowledgements. This work has been partially funded by the Bundesministerium für Wirtschaft und Energie under the Deutsches Zentrum für Luft- und Raumfahrt Grants 50 OR 1915. The research leading to these results has received funding from the European Union's Horizon 2020 Programme under the AHEAD2020 project (grant agreement n. 871158) and from the ESA Archival Research Visitor Programme. SMN acknowledges funding under project PID2021-122955OB-C41 funded by MCIN/AEI/10.13039/501100011033 and by 'ERDF A way of making Europe'. RA acknowledges support by the CNES. Work at LLNL was performed under the auspices of the US Department of Energy under contract No. DE-AC52-07NA27344 and supported through NASA grants to LLNL. This work has made use of (1) the Interactive Spectral Interpretation System (ISIS) maintained by Chandra X-ray Center group at MIT; (2) the *NuSTAR* Data Analysis Software (NuSTARDAS) jointly developed by the ASI Science Data Center (ASDC, Italy) and the California Institute of Technology (Caltech, USA); (3) the ISIS functions (`isisscripts`)[6] provided by ECAP/Remeis observatory and MIT; (4) NASA's Astrophysics Data System Bib-

[5] https://heasarc.gsfc.nasa.gov/xstar/docs/html/node102.html

[6] http://www.sternwarte.uni-erlangen.de/isis/

liographic Service (ADS); (5) the Users Guide to the XMM-Newton Science Analysis System, Issue 17.0, 2022 (ESA: XMM-Newton SOC). We thank John E. Davis for the development of the `slxfig`[7] module used to prepare most of the figures in this work. Others were created with the Veusz[8] package. WebPlotDigitizer[9] (© Ankit Rohatgi) has been used to digitise data from figures in older publications.

References

Amato, R., Grinberg, V., Hell, N., et al. 2021, A&A, 648, A105
Arnaud, K. A. 1996, Astronomical Society of the Pacific Conference Series, Vol. 101, XSPEC: The First Ten Years, ed. G. H. Jacoby & J. Barnes, 17
Astropy Collaboration, Price-Whelan, A. M., Lim, P. L., et al. 2022, ApJ, 935, 167
Bachetti, M., Huppenkothen, D., Khan, U., et al. 2022, StingraySoftware/stingray: v1.0-beta
Barret, D., Decourchelle, A., Fabian, A., et al. 2020, Astronomische Nachrichten, 341, 224
Becker, R. H., Rothschild, R. E., Boldt, E. A., et al. 1978, ApJ, 221, 912
Bildsten, L., Chakrabarty, D., Chiu, J., et al. 1997, ApJS, 113, 367
Blondin, J. M. 1994, in American Institute of Physics Conference Series, Vol. 308, The Evolution of X-ray Binariese, ed. S. Holt & C. S. Day, 578
Blondin, J. M., Kallman, T. R., Fryxell, B. A., & Taam, R. E. 1990, ApJ, 356, 591
Blondin, J. M., Stevens, I. R., & Kallman, T. R. 1991, ApJ, 371, 684
Conti, P. S. 1978, A&A, 63, 225
den Herder, J. W., Brinkman, A. C., Kahn, S. M., et al. 2001, A&A, 365, L7
Diez, C. M., Grinberg, V., Fürst, F., et al. 2022, A&A, 660, A19
Drake, G. W. 1988, Canadian Journal of Physics, 66, 586
El Mellah, I., Grinberg, V., Sundqvist, J. O., Driessen, F. A., & Leutenegger, M. A. 2020, A&A, 643, A9
Erickson, G. W. 1977, Journal of Physical and Chemical Reference Data, 6, 831
Falanga, M., Bozzo, E., Lutovinov, A., et al. 2015, A&A, 577, A130
Fransson, C. & Fabian, A. C. 1980, A&A, 87, 102
Fürst, F., Kreykenbohm, I., Pottschmidt, K., et al. 2010, A&A, 519, A37
Fürst, F., Pottschmidt, K., Wilms, J., et al. 2014a, ApJ, 784, L40
Fürst, F., Pottschmidt, K., Wilms, J., et al. 2014b, ApJ, 780, 133
Fürst, F., Suchy, S., Kreykenbohm, I., et al. 2011, A&A, 535, A9
Garcia, J. D. & Mack, J. E. 1965, Journal of the Optical Society of America (1917-1983), 55, 654
Giménez-García, A., Shenar, T., Torrejón, J. M., et al. 2016, A&A, 591, A26
Gokus, A. 2017, Broadband emission processes of Active Galactic Nuclei
Goldstein, G., Huenemoerder, D. P., & Blank, D. 2004, AJ, 127, 2310
Grinberg, V., Hell, N., El Mellah, I., et al. 2017, A&A, 608, A143
Grinberg, V., Nowak, M. A., & Hell, N. 2020, A&A, 643, A109
Haberl, F. & White, N. E. 1990, ApJ, 361, 225
Heinz, S., Burton, M., Braiding, C., et al. 2015, ApJ, 806, 265
Hell, N., Brown, G. V., Wilms, J., et al. 2016, ApJ, 830, 26
HI4PI Collaboration, Ben Bekhti, N., Flöer, L., et al. 2016, A&A, 594, A116
Hiltner, W. A., Werner, J., & Osmer, P. 1972, ApJ, 175, L19
Hirsch, M., Hell, N., Grinberg, V., et al. 2019, A&A, 626, A64
Houck, J. C. & Denicola, L. A. 2000, Astronomical Society of the Pacific Conference Series, Vol. 216, ISIS: An Interactive Spectral Interpretation System for High Resolution X-Ray Spectroscopy, ed. N. Manset, C. Veillet, & D. Crabtree, 591
House, L. L. 1969, ApJS, 18, 21
Huppenkothen, D., Bachetti, M., Stevens, A., et al. 2019, Journal of Open Source Software, 4, 1393
Huppenkothen, D., Bachetti, M., Stevens, A. L., et al. 2019, ApJ, 881, 39
Jansen, F., Lumb, D., Altieri, B., et al. 2001, A&A, 365, L1
Jethwa, P., Saxton, R., Guainazzi, M., Rodriguez-Pascual, P., & Stuhlinger, M. 2015, A&A, 581, A104
Joss, P. C. & Rappaport, S. A. 1984, ARA&A, 22, 537
Kaastra, J. S. & Bleeker, J. A. M. 2016, A&A, 587, A151
Kallman, T. R. & McCray, R. 1982, ApJS, 50, 263
Kendziorra, E., Mony, B., Kretschmar, P., et al. 1992, in Frontiers Science Series, ed. Y. Tanaka & K. Koyama, 51
Kretschmar, P., El Mellah, I., Martínez-Núñez, S., et al. 2021, A&A, 652, A95
Kretschmar, P., Pan, H. C., Kendziorra, E., et al. 1997, A&A, 325, 623
Kreykenbohm, I., Coburn, W., Wilms, J., et al. 2002, A&A, 395, 129
Kreykenbohm, I., Kretschmar, P., Wilms, J., et al. 1999, A&A, 341, 141
Kreykenbohm, I., Wilms, J., Kretschmar, P., et al. 2008, A&A, 492, 511
Lai, E. V., De Marco, B., Zdziarski, A. A., et al. 2022, MNRAS, 512, 2671
Lewis, W., Rappaport, S., Levine, A., & Nagase, F. 1992, ApJ, 389, 665
Lomaeva, M., Grinberg, V., Guainazzi, M., et al. 2020, A&A, 641, A144
Madsen, K. K., Grefenstette, B. W., Pike, S., et al. 2020, arXiv e-prints, arXiv:2005.00569
Malacaria, C., Mihara, T., Santangelo, A., et al. 2016, A&A, 588, A100
Manousakis, A. & Walter, R. 2015a, A&A, 575, A58
Manousakis, A. & Walter, R. 2015b, A&A, 584, A25
Manousakis, A., Walter, R., & Blondin, J. M. 2012, A&A, 547, A20
Martínez-Núñez, S., Kretschmar, P., Bozzo, E., et al. 2017, Space Sci. Rev., 212, 59
Martínez-Núñez, S., Torrejón, J. M., Kühnel, M., et al. 2014, A&A, 563, A70
Nagase, F., Zylstra, G., Sonobe, T., et al. 1994, ApJ, 436, L1
Nowak, M. A., Hanke, M., Trowbridge, S. N., et al. 2011, ApJ, 728, 13
Ohashi, T., Inoue, H., Koyama, K., et al. 1984, PASJ, 36, 699
Orlandini, M., Dal Fiume, D., Frontera, F., et al. 1998, A&A, 332, 121
Pintore, F., Sanna, A., Di Salvo, T., et al. 2014, MNRAS, 445, 3745
Quaintrell, H., Norton, A. J., Ash, T. D. C., et al. 2003, A&A, 401, 313
Rawls, M. L., Orosz, J. A., McClintock, J. E., et al. 2011, ApJ, 730, 25
Sako, M., Liedahl, D. A., Kahn, S. M., & Paerels, F. 1999, ApJ, 525, 921
Sato, N., Hayakawa, S., Nagase, F., et al. 1986, PASJ, 38, 731
Schulz, N. S., Canizares, C. R., Lee, J. C., & Sako, M. 2002, ApJ, 564, L21
Staubert, R., Trümper, J., Kendziorra, E., et al. 2019, A&A, 622, A61
Strüder, L., Briel, U., Dennerl, K., et al. 2001, A&A, 365, L18
Tiesinga, E., Mohr, P. J., Newell, D. B., & Taylor, B. N. 2021, Rev. Mod. Phys., 93, 025010
Tsygankov, S. S., Rouco Escorial, A., Suleimanov, V. F., et al. 2019, MNRAS, 483, L144
Turner, M. J. L., Abbey, A., Arnaud, M., et al. 2001, A&A, 365, L27
van Kerkwijk, M. H., van Paradijs, J., & Zuiderwijk, E. J. 1995, A&A, 303, 497
Verner, D. A., Ferland, G. J., Korista, K. T., & Yakovlev, D. G. 1996, ApJ, 465, 487
Watanabe, S., Sako, M., Ishida, M., et al. 2006, ApJ, 651, 421
Wilms, J., Allen, A., & McCray, R. 2000, ApJ, 542, 914
XRISM Science Team. 2020, arXiv e-prints, arXiv:2003.04962

[7] http://www.jedsoft.org/fun/slxfig/
[8] https://veusz.github.io/
[9] https://automeris.io/WebPlotDigitizer/

Appendix A: Calibration of *XMM-Newton* EPIC-pn timing mode

In this section, we discuss the calibration of the *XMM-Newton* EPIC-pn timing mode and the tests we performed to justify our choice of calibration and data extraction for this work. We discuss our tests and their implications to conclude with the possible caveats.

A.1. Test for RDCTI and RDPHA correction in the iron line region

When processing the ODFs to obtain calibrated and concatenated event lists to later generate scientific products, one has to use the `epproc` task. The default calibration of this task for timing mode data[1] uses `withrdpha='Y'`, `withxrlcorrection='Y'`, `runepreject='Y'`, `runepfast='N'`; `Y` and `N` standing for `YES` and `NO`, respectively.

The Rate-Dependent PHA (RDPHA) correction was introduced with SASv13 as a more robust method than the Rate-Dependent CTI (RDCTI) correction to rectify count-rate-dependent effects on the energy scale of EPIC-pn exposures in timing mode[10]. Thus, the task `epfast`, which applies the RDCTI correction, does not run on data that have been already corrected with the RDPHA correction, and vice versa. This explains why `runepfast` is set to `'N'`, because `withrdpha` is set to `'Y'` by default in the timing mode.

However, when extracting the *XMM-Newton* EPIC-pn spectra for this Vela X-1 observation with the timing mode default RDPHA correction, we obtained higher energies than expected for the line features in the 0.5–10 keV energy range covered by EPIC-pn. This is particularly visible for the fluorescent emission line associated with FeKα as it is the most prominent emission feature in the spectrum of Vela X-1. Figure A.1 shows an example of a spectrum with the RDPHA correction in the iron line region fitted with a simple power law and a Gaussian component. The FeKα line is found at more than 6.53 keV, while it is expected to be located around ~6.4 keV according to our results of the simultaneous *NuSTAR* observation (Diez et al. 2022) or in the spectrum of Vela X-1 in general (see e.g. Goldstein et al. 2004; Watanabe et al. 2006; Giménez-García et al. 2016). The energy of the iron line also depends on how much the observation is affected by pile-up; this aspect is discussed in the following section.

In order to perform a sanity check of the RDPHA correction, we decided to revert back to the RDCTI correction (`epfast`), as this latter was usually performed in timing mode before the RDPHA correction got released in SASv13 and later versions (Martínez-Núñez et al. 2014). We therefore tested `epproc` running the `epfast` task, therefore using the parameters `withdefaultcal='N'`, `withrdpha='N'`, `withxrlcorrection='Y'`, `runepreject='Y'`, `runepfast='Y'`. This setting corresponds to the default calibration of the burst mode[1]. This results in an iron line around 6.34 keV as presented in Fig. A.1, which is more consistent with what we expected. The shift we obtained between the two calibrations is of ~140 eV, which may impact the quality of our results. It was also seen in the instrumental line features of the detector such as the gold edge region around ~2.2 keV. The same behaviour was seen by Pintore et al. (2014) in the spectra of the accreting neutron star GX 13+1, where the authors found a shift of 360 eV in the iron line between the RDCTI and RDPHA corrections.

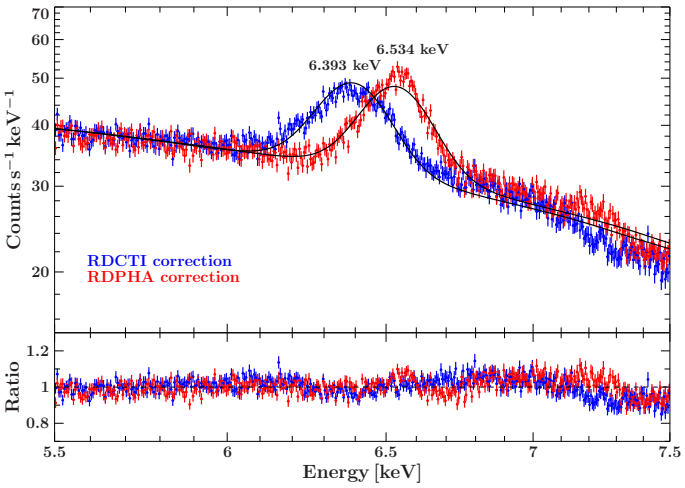

Fig. A.1. Example of a spectrum in the iron line region generated with different calibrations. The red spectrum corresponds to events generated applying the RDPHA correction, while the blue spectrum corresponds to the RDCTI correction.

A.2. Test for pile-up in the iron line region

As mentioned in Sect. 2, our *XMM-Newton* EPIC-pn observation of Vela X-1 is deeply affected by pile-up. In addition, with the `epatplot` task, we evaluate the pixel columns most affected by pile-up by performing a test in the iron line region. We extract spectra ignoring 1, 3, 5, and 7 columns from the PSF centre (named PSF–#) and then compare the position of the iron line between different extractions. We present example spectra as in Fig. A.1, using the RDPHA correction (see Fig. A.2) and RDCTI correction (see Fig. A.3), where we fitted with a power law and Gaussian component to model the iron line.

We note that with the RDPHA correction, the more the centremost columns are removed, the lower the energy of the iron line is starting from ~6.54 keV for one column removed to ~6.50 keV for seven ignored columns. However, removing seven columns from the centre of the PSF means ignoring almost the entire available signal, decreasing the S/N. Moreover, the iron line energy is still too high compared to what we expect for this feature as discussed in Sect. A.1. On the contrary, using the RDCTI correction, we obtain the opposite behaviour, with an increase in the iron line energy together with the number of centre columns removed from the PSF. In order to have a good balance between keeping enough signal and having a consistent iron line energy with previous results for Vela X-1, we decided to apply the RDCTI correction and to remove the three centremost columns from the PSF (PSF–3) for this work. Even if we apply those corrections, the energy of the iron line (~6.46 keV) is still higher than what we obtained for the simultaneous *NuSTAR* observation, and so discrepancies between the two instruments are expected for the combined spectral analysis presented in Sect. 4.2.

[10] see the CCF Release Note 0312 (Guainazzi M., 2014a, XMM-CCF-REL-0312) https://xmmweb.esac.esa.int/docs/documents/CAL-SRN-0312-1-4.pdf and the Science Operations Team Calibration Technical Note 0083 (Guainazzi M., et al. 2014b, XMM-SOC-CAL-TN-0083) https://xmmweb.esac.esa.int/docs/documents/CAL-TN-0083.pdf

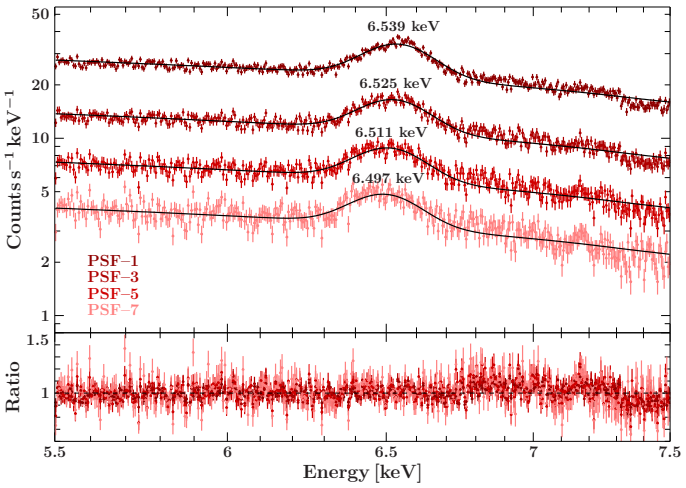

Fig. A.2. Example of a spectrum with RDPHA correction as in Fig. A.1, removing 1 (PSF–1), 3 (PSF–3), 5 (PSF–5), and 7 (PSF–7) columns from the centre of the PSF.

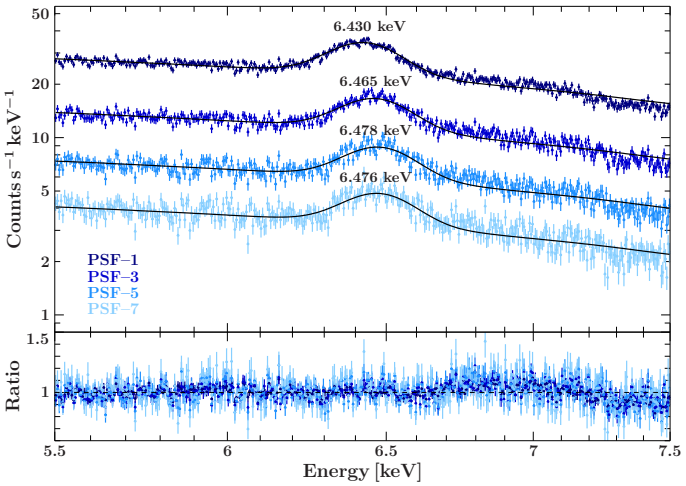

Fig. A.3. Example of a spectrum with RDCTI correction as in Fig. A.1 removing 1 (PSF–1), 3 (PSF–3), 5 (PSF–5), and 7 (PSF–7) columns from the centre of the PSF.

A.3. Cross-instrumental issues

In comparison with *XMM-Newton* EPIC-pn data, we observe a strong soft excess in the *NuSTAR* data (see Fig. A.4). A possible explanation for this is the dust scattering effect. In this scenario, we suppose dense interstellar clouds located between the observer and the source. Those clouds will lead to deviation of the trajectory of low-energy photons that were not supposed to be observed. The low-energy photons will then be scattered towards the observer, producing a soft excess flux at low energy in the spectrum of the source. This scattering leads to the formation of the scattering halo as observed in Circinus X-1 in Heinz et al. (2015). To check for this phenomenon, we extracted source regions of different sizes in the *NuSTAR* data from 10 arcsec to 50 arcsec is steps of 10 arcsec. The smallest source regions account for the maximum of the PSF, though with a possible loss of information from the source. The largest source regions account for the PSF and outside wings, which is where the dust scattering effect is visible and more low-energy photons are present. When comparing the resultant spectra, we cannot see any difference in terms of spectral shape, meaning the soft excess at low energy is always present. Hence, we exclude the dust scattering effect as a cause for the observed soft excess in our *NuSTAR* data. We also checked for contamination sources in the extracted source region of both instruments but none could be found. As we are unable to find a plausible physical explanation for this phenomenon, we tested our model by tying CF_{NuSTAR} to CF_{XMM}. In the second residual panel of Fig. A.4, we observe that the *XMM-Newton* EPIC-pn data are well described, albeit the residuals increase drastically for *NuSTAR* around 3 keV. Reciprocally, we tied CF_{XMM} to CF_{NuSTAR} and, as expected, the *NuSTAR* data are well constrained. However, there is a discrepancy up to a factor of 10 between the model and the *XMM-Newton* EPIC-pn data at 0.5 keV as shown on the last residual panel of Fig. A.4. None of the datasets are correctly described by an averaged CF. We conclude that the CF_{XMM} is the most reliable value for the covering fraction and that the problem may be due to remaining calibration effects from *NuSTAR* at low energies. For the rest of this work, we assumed two independent CFs for each instrument as this is the best way to empirically compensate for the observed difference (see the first residual panel of Fig. A.4). In Tsygankov et al. (2019), an offset between *Swift*/XRT and *NuSTAR* has also been reported. The *Swift*/XRT normalisation was about 1.3 times lower than *NuSTAR* FPMA/FPMB, which is possibly due to the fact that their *NuSTAR* and *Swift* observations were not strictly simultaneous.

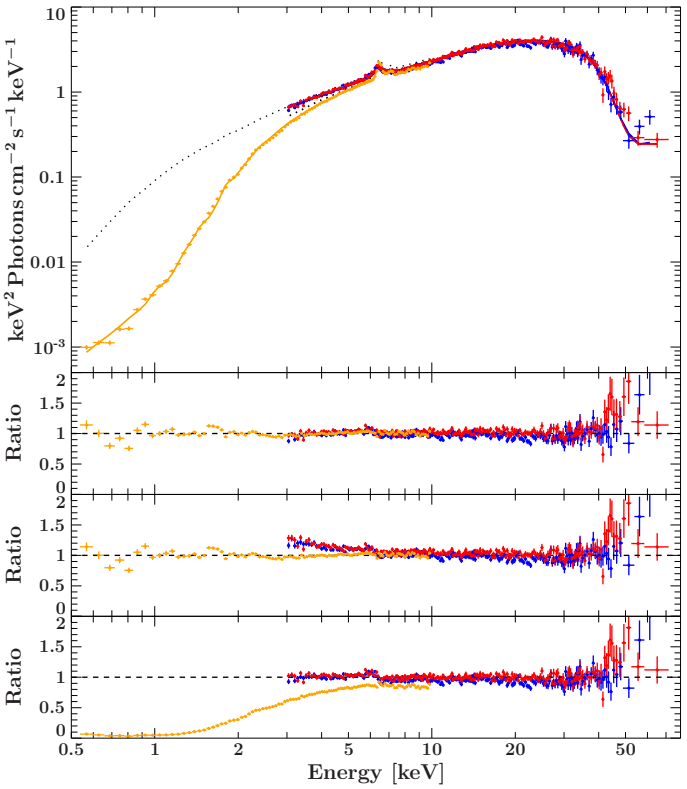

Fig. A.4. Example of an unfolded spectrum taken with *XMM-Newton* EPIC-pn (orange), *NuSTAR* FPMA (red), and FPMB (blue) during the fourth *NuSTAR* orbit. Solid lines show the best-fit model with independent CF_{XMM} and CF_{NuSTAR}, and dotted lines account for best-fit model with tied CFs. First residual panel: Best-fit model with independent covering fractions. Second residual panel: Best-fit model with CF_{NuSTAR} tied to CF_{XMM}. Last residual panel: Best-fit model with CF_{XMM} tied to CF_{NuSTAR}. A strong soft excess in the *NuSTAR* data is visible at ~3 keV in comparison to the *XMM-Newton* data.